ACS OMEGA

http://pubs.acs.org/journal/acsodf

Article

# Exciton Lifetime Distributions and Population Dynamics in the FMO Protein Complex from *Prosthecochloris aestuarii*

Tonu Reinot, Anton Khmelnitskiy, Adam Kell, Mahboobe Jassas, and Ryszard Jankowiak*

Cite This: *ACS Omega* 2021, 6, 5990−6008

Read Online

ACCESS | Metrics & More | Article Recommendations | Supporting Information

**ABSTRACT:** Significant protein rearrangement upon excitation and energy transfer in Fenna−Matthews−Olson protein of *Prosthecochloris aestuarii* results in a modified energy landscape, which induces more changes in pigment site energies than predicted by the "standard" hole-burning theory. The energy changes are elucidated by simulations while investigating the effects of site-dependent disorder, both static (site-energy distribution widths) and dynamic (spectral density shapes). The resulting optimized site energies and their fluctuations are consistent with relative differences observed in inhomogeneous widths calculated by recent molecular dynamic simulations. Two sets of different spectral densities reveal how their shapes affect the population dynamics and distribution of exciton lifetimes. Calculations revealed the wavelength-dependent distributions of exciton lifetimes ($T_1$) in the femtosecond to picosecond time frame. We suggest that the calculated multimodal and asymmetric wavelength-dependent $T_1$ distributions offer more insight into the interpretation of resonant hole-burned (HB) spectra, kinetic traces in two-dimensional (2D) electronic spectroscopy experiments, and widely used global analyses in fitting data from transient absorption experiments.

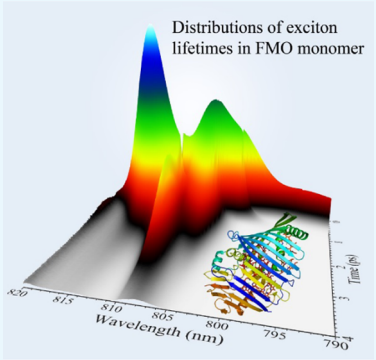


## 1. INTRODUCTION

The well-studied Fenna−Matthews−Olson (FMO) protein homotrimer binds a minimum of seven bacteriochlorophyll (BChl) molecules per monomer, as confirmed by multiple crystal structures over the years.[1−6] An eighth BChl *a* pigment in *Chlorobaculum tepidum* FMO has been resolved at the interface between monomers[2] but with variable occupancy (based on X-ray crystallography and oxidation experiments).[7,8] However, a very recent structure of *Prosthecochloris aestuarii* FMO resolved only seven BChls per monomer.[3] In fact, all *P. aestuarii* samples studied in our laboratory contained only seven BChls per monomer. The eighth pigment is either lost during protein isolation and/or purification procedures.[2] Although several spectral assignments for BChl *a*, based on the simulations of various optical spectra[9−14] or theoretical calculations[13,15−18] have been proposed, the pigment site energies, energy landscape, and excitation energy transfer (EET) pathways in the *P. aestuarii* FMO complex are not fully determined. In particular, it is not obvious whether all monomer pigments have different shapes of phonon spectral densities. Nevertheless, there is an overwhelming consensus that BChl *a* 3 is the lowest energy pigment,[8,9,12,17−19] being located near the membrane-bound reaction center (RC),[2] and that BChl *a* 4 has minor contribution to the lowest energy state.[8,20] It is assumed that pigments near the baseplate most likely contribute to the high-energy states;[15] however, assignments of the site energies of BChls are not well established. This is especially true of *P. aestuarii* FMO, which has been studied less in recent years than *Calosoma tepidum* FMO.

There is also no consensus as to the origin and nature of the resonant and nonresonant hole-burned (NRHB) spectra, although various interpretations have been proposed.[21−24] In general, there are differences between the shapes of the reported absorption, circular dichroism (CD), emission, and NRHB spectra[12,25] complicating the proper assignment of BChl site energies in *P. aestuarii* FMO complexes. Therefore, heterogeneity of the isolated FMO complexes and the efficiency of uncorrelated EET between monomers need to be considered before the differences observed between the nonresonant and resonant HB spectra are assigned to processes responsible for observed spectral features, as suggested in ref 21. For example, it was proposed that the broad absorbance changes and the relatively sharp features (resonant with the burn wavelength) are induced by different mechanisms, with the former likely due to protein conformational changes.[21] Furthermore, the small features (bleaches) observed in ref 23 and assigned to the energy levels of the individual exciton states in the $Q_y$ band were not reproduced in ref 21.

Very recently, it was demonstrated experimentally by two-dimensional electronic spectroscopy (2DES) that the short lifetime of electronic coherence in FMO, LHCII, and PSII RC

**Received:** January 20, 2021
**Accepted:** February 9, 2021
**Published:** February 19, 2021

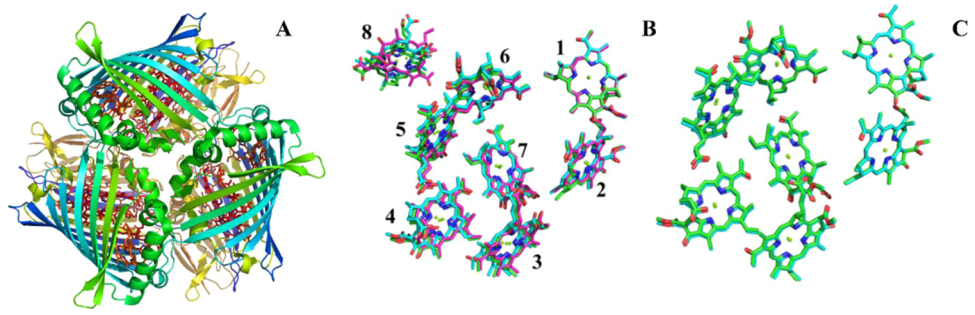


**Figure 1.** (A) FMO trimer of *P. aestuarii* based on the 6MEZ protein data file.[3] (B) Alignment of atomic coordinates for BChl *a* molecules of the FMO monomer from *C. tepidum* (green),[2] *P. aestuarii* (cyan),[3] and *P. phaeum* (magenta).[6] (C) Comparison of BChl *a* 1−7 coordinates for the 3EOJ (green) and 6MEZ (cyan) *P. aestuarii* structures (we do not show phytyl tails for clarity). Figure created with PyMOL.

complexes prevents the development of long-lived oscillations related to exciton coherence and is unimportant with respect to the EET in the typical photosynthetic protein complexes at ambient temperature.[26] However, numerous previously published papers revealed different dynamics of excitonic populations and coherence, both experimentally[27,28] and theoretically.[29,30] Thus, the lack or presence of long-lived quantum coherence in EET in *P. aestuarii* complexes is still a matter of debate[31] and more information on the excitonic structure is needed. Resonant HB experiments of *C. tepidum* FMO and its mutants suggest that relaxation of low-energy and high-energy exciton states occurs on a picosecond and subpicosecond time scale, respectively.[20,32,33]

We studied many *P. aestuarii* complexes during the last decade to address their intactness and/or heterogeneity,[20,34] as well as the controversial issues mentioned above. In this work, we apply HB spectroscopy and modeling studies of absorption, emission, CD, and resonant/NRHB spectra to provide more insight into its excitonic structure and dynamics. Here, we only note that *P. aestuarii* displays type 1 absorption spectra (where the 12 280 $cm^{-1}$ band is most intense) and *C. tepidum* displays a type 2 absorption spectrum (with the 12 400 $cm^{-1}$ band carrying most intensity), although these complexes are structurally very similar.[1,3] Figure 1A shows FMO trimer of *P. aestuarii*. Figure 1B illustrates high structural homology between FMO complexes of FMO from *C. tepidum* (green), *P. aestuarii* (cyan), and *Pelodictyon phaeum* (magenta). These complexes, based on ref 2, contain eight BChls per monomer. Although phytyl tails have been truncated for clarity, the alignment algorithm of crystal structures took phytyl tails into consideration when minimizing the root-mean-square deviation. It is apparent that the arrangements of the BChls in all three FMO complexes are very similar. The latter, however, does not mean that all FMO complexes have the same energy landscape and/or propensity to light-induced protein conformational changes. A comparison of monomer structures of the *P. aestuarii* FMO with only seven BChls,[3] i.e., the 3EOJ (green; BChl 8 is not shown) and 6MEZ (cyan) structures, is shown in Figure 1C.

Below, we describe the spectral differences observed in *P. aestuarii* FMO trimers and discuss various Hamiltonians that can simultaneously describe multiple optical spectra, including HB spectra obtained for our intact complexes. We discuss the influence of the number and shape of phonon spectral densities (SDs) for individual pigments on exciton population dynamics, exciton lifetimes, and temperature dependence of absorption spectra (for comparison, we show Hamiltonians describing the absorption and CD spectra of Vulto et al.[12] in the Supporting Information). Finally, the recently calculated site energies and site inhomogeneities of individual pigments[17,18] are contrasted with the parameters obtained from our modeling studies. The main objective, however, is to provide insight into population dynamics and to distinguish between regular HB and possible additional light-induced protein conformational changes, both experimentally and via modeling studies. In particular, we show below that: (i) due to site-dependent fluctuations static disorder at 5 K is site-specific, i.e., inhomogeneous broadening varies from pigment to pigment, but it is much smaller than that calculated by recent molecular dynamic (MD) simulations at room temperature;[17,18] (ii) we argue that in all FMO samples from *P. aestuarii* studied in this laboratory BChl 8 is absent; (iii) we provide further evidence that the site energy of BChl 8 most likely lies near 805−806 nm, in agreement with refs 8, 18, and 35, not near 780−787 nm as suggested in refs 9 and 17; (iv) we suggest that the Drude−Lorentz shapes of phonon SDs cannot describe the experimentally observed low-temperature phonon sideband; (v) we reason that the exciton population dynamics must be consistent with both time- and frequency-domain data, reflecting experimentally observed picosecond and femtosecond exciton lifetimes;[28,36−38] and (vi) we suggest that the shape of *P. aestuarii* FMO NRHB spectra are affected by long-range protein conformational changes not present in *C. tepidum* FMO.

## 2. MATERIALS AND METHODS

**2.1. Sample Preparation.** Isolated FMO complexes were prepared as described previously[39,40] with a 50 mM Tris-HCl buffer and stored at 0 °C. All samples over the years were prepared by students and postdocs in Prof. R. Blankenship laboratory. A glass-forming solution of glycerol and ethylene glycol (55/45 v/v) was added to all samples before low-temperature experiments.

**2.2. Experimental Procedures.** A Bruker HR125 Fourier transform spectrometer was used to measure low-temperature absorption and HB spectra. In absorption and NRHB measurements, the resolution was set to 4 $cm^{-1}$, while for resonant HB, a spectral resolution of 1 $cm^{-1}$ was used. Fluorescence spectra were collected with a resolution of 0.1 nm by a Princeton Instruments Acton SP-2300 spectrograph equipped with a back-illuminated CCD camera (PI Acton Spec10, 1340 × 400). The excitation source for both NRHB and fluorescence spectra was 488.0 and/or 496.5 nm laser lines from a Coherent Innova-90 argon ion laser. In resonant HB experiments, the tunable excitation came from a Coherent 899-01 Ti:Sapphire laser (line width of 0.07 $cm^{-1}$) pumped by a Millenia 10s (Spectra-Physics) diode-pumped solid-state laser at 532 nm. Power from the laser output was stabilized with a Laser Power Controller (Brockton Electro-Optics Corp.) and


https://dx.doi.org/10.1021/acsomega.1c00286
ACS Omega 2021, 6, 5990−6008

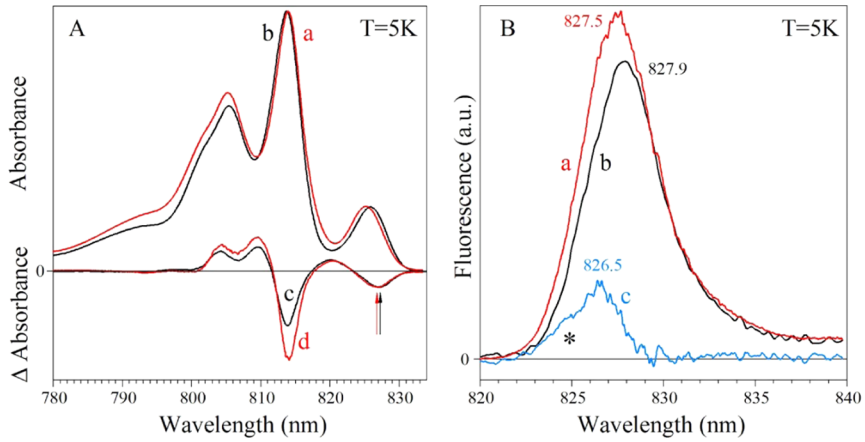


**Figure 2.** Comparison of typical intact (black; b) and destabilized (red; a) spectra of *P. aestuarii* FMO at 5 K. (A) Absorption (curves a and b) and NRHB spectra (c and d, $\lambda_B$ = 488.0 nm) normalized to the low-energy band/hole. The spectral resolution is 4 $cm^{-1}$. Curves b and c correspond to our best FMO sample. Color-coded arrows indicate the lowest band maxima in NRHB spectra. (B) Color-coded emission spectra a and b correspond to the absorption spectra a and b shown in the left panel. Curve c is the difference between spectra a and b (see text for details). Asterisk marks the location of monomer contribution to the emission.

precisely set by a continuously adjustable neutral density filter. All experiments were performed inside a Janis 8-DT Super Vari-Temp liquid helium cryostat controlled by a Lakeshore Cryotronic model 330 temperature controller.

**2.3. Modeling Studies.** Our modeling approach is described in ref 8 and Section S1 of the Supporting Information. In brief, the disorder is introduced into the diagonal matrix elements (i.e., $E_0^n$) by a Monte-Carlo approach with normal distributions centered at $E_0^n$ ($n$ labeling various pigments, i.e., $n$ = 1−21 or 1−24) and with full width at half maximum (fwhm) representing $\Gamma_{inh}$, which can be site dependent. Eigendecomposition of the interaction matrix provides eigencoefficients ($c_n^M$) and eigenvalues ($\omega_M$). Phonon and vibrational Huang−Rhys factors ($S$), used as free parameters, are optimized simultaneously against the experimental spectra. In model I, we assume that the phonon spectral density (weighted phonon profile) is well described by a continuous function, which is chosen to be a lognormal distribution, as illustrated in ref 41. We use experimentally determined phonon spectral density $J_{ph}(\omega)$[41,42] for BChl 3 and a broader spectral density shape for the remaining pigments (for details see refs 8 and 41), and vibrational spectral density $J_{vib}(\omega)$.[42] Intramolecular vibrational modes ($J_{vib}$) are considered to be dynamically localized.[43] $S_{ph}$ = 0.4 while the total sum of all individual vibration $S$-factors, $S_{vib}$ = 0.17 and 0.3 for absorption and emission spectra, respectively. In model II, we use modified Drude−Lorentz SDs; details are given below and in the Supporting Information.

In simulations of optical spectra, we use a non-Markovian reduced density matrix theory[44] with a Nelder−Mead simplex algorithm for parameter optimization.[45] Our in-house written software can simultaneously fit several types of experimental spectra at different temperatures, providing constraints on the pigment site energies of interest. We model NRHB spectra in the following way; after diagonalization of the Frenkel Hamiltonian, a preburn absorption spectrum is calculated from Redfield theory.[44,46] The low-fluence approximation is used, which allows to burn (change energy) only for pigments that contribute to the thermally allowed lowest energy exciton states. That is, we select the burning pigment randomly, in proportion to pigments' thermal occupation numbers. The latter are calculated by finding thermal occupation numbers for each exciton state, followed using squared eigenvectors to sum pigment contributions to these states. The postburn site energy of the burned pigment is selected randomly either from the same site-distribution function (SDF) or, if the energy landscape is modified, the distribution's width and mean can change. All other diagonal elements of the Hamiltonian are unchanged. The Hamiltonian is again diagonalized and a postburn absorption spectrum is calculated. The resulting HB spectrum is calculated as the preburn absorption subtracted from the postburn absorption spectrum. However, our algorithm allows additional site-energy changes for some or all of the pigments (with variable probability) to describe the experimentally observed spectral changes (see Section 4.4). Each calculated spectrum is a result of 400 000 accumulated Monte-Carlo realizations and Gaussian smoothing (fwhm = 11 $cm^{-1}$). Exciton lifetimes ($T_1$) are calculated from exciton line widths using Redfield theory (see the Supporting Information); $T_1$ values are averaged and plotted as a function (histogram) of exciton energy. The spectral resolution for calculations is 1 $cm^{-1}$, which is also the bin size of the histogram. $T_1$ distributions (averaged over a desired wavelength range) are plotted as a function of time; in this case, the binning width is 2 fs and the total time range is 0−20 ps. Each exciton lifetime distribution is a result of 50 000 000 Monte-Carlo realizations.

## 3. RESULTS

**3.1. Experimental Results.** *3.1.1. Absorption and Fluorescence Spectra.* Figure 2A shows typical differences observed in the absorption and nonresonant HB spectra ($\lambda_B$ = 496.5 nm) of *P. aestuarii* samples measured in our laboratory at $T$ = 5 K during the last decade. Spectra of partly destabilized and our best (most intact) FMO complexes are shown as curves a and b, respectively. While the first and third absorption bands in curve a shift blue by about 0.5 nm, the second band near 814 nm shifts slightly red. The corresponding nonresonant HB spectra (curves d and c, respectively) are also different. Noticeably, the depth of the hole near 814 nm (~12 280 $cm^{-1}$) in the partly destabilized complexes (curve d) is deeper when spectra are normalized to the low-energy hole at 827.1 nm (12 090 $cm^{-1}$). Remarkably, absorption near 806.5 nm (12 400 $cm^{-1}$) in curve a has larger oscillator strength than curve b, possibly due to a small contribution from BChl 8 in this particular sample, though


https://dx.doi.org/10.1021/acsomega.1c00286
ACS Omega 2021, 6, 5990−6008

slightly different baseline could also account (at least in part) for this effect. However, the overall shapes of nonresonant HB spectra (sample-dependent) are consistent with earlier studies.[21,32] Our extensive studies of multiple *P. aestuarii* FMO samples during the last decade suggest that, in general, the blue-shifted spectra are likely due to sample destabilization.

So far there were no attempts to describe the HB spectra theoretically. We hasten to add that the absorption spectra of aged complexes (kept in the freezer for 1−3 years), again with variable oscillator strength near 805−807 nm, are similar to spectrum a in Figure 2A suggesting that partial destabilization can also occur during extended storage (spectra not shown for brevity). It appears that *P. aestuarii* FMO trimers, as previously reported for *C. tepidum* FMO,[34] also exhibit sample-dependent shifts of absorption, emission, and HB spectra. The differences between spectra a and b shown in Figure 2 (as well as HB spectra; curves d and c, respectively) are discussed in Section 4.1. Since the ∼825 nm absorption bands in spectra a and b in Figure 2A are slightly shifted, the emission spectra originating from the corresponding lowest energy state should also be shifted with somewhat different shapes, in particular, when destabilization would affect the efficiency of the EET between monomers of the trimer. This is indeed observed, i.e., Figure 2B shows that the emission spectrum obtained for partly destabilized FMO (curve a) is broader and blue-shifted in comparison with spectrum b obtained for intact FMO (with a maximum near 827.5 nm). Curve c is the difference between spectra a and b, which is assigned (at least in part) to the emission from the destabilized complexes with a maximum near 826.5 nm.

*3.1.2. Hole-Burned (HB) Spectra Burned at $\nu_B$ = 12 284 cm$^{-1}$.* Curves b−f in Figure 3 are HB spectra burned at the maximum of the most intense absorption band near 814 nm of the FMO trimer with an increasing fluence. The HB spectra consist of a ZPH at the burning frequency and a broad NRHB spectrum due to EET to the lowest energy exciton state. That is, the bleach of the lowest energy exciton state occurs after light-induced coherences vanish and uncorrelated Förster-type EET between the lowest energy excitons of the three monomers (of the intact FMO trimers) takes place.

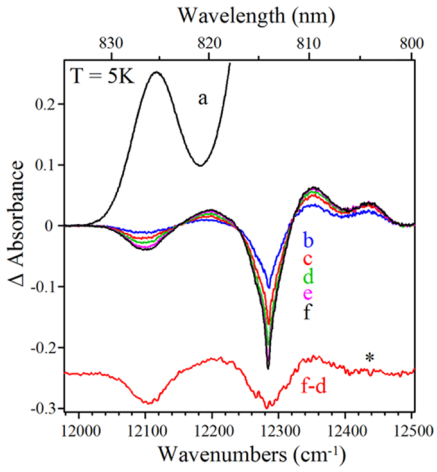


**Figure 3.** Figure shows 5 K absorption (curve a) and resonant ($\nu_B$ = 12 284 cm$^{-1}$) HB spectra (curves b−f) of *P. aestuarii* FMO as a function of burning fluence from 0.5 to 4 J/cm$^2$. The red curve in the bottom is shifted apart for clarity and amplified ×4. It is the difference between spectra f and d with the ZPH subtracted. An asterisk indicates the location of a band that forms in the beginning phase of hole burning (see text).

The red curve, f − d, at the bottom of Figure 3 is the difference between spectra f and d with ZPH subtracted. Interestingly, this curve reveals a typical nonresonant bleach (similar to that observed in *C. tepidum* FMO)[34] with a smaller ratio of 814 to 827 nm bleach (in contrast with curve c in Figure 2A). Moreover, in contrast to HB spectra shown in Figure 3, the (f − d) difference spectrum does not show the positive band near 12 440 cm$^{-1}$ (803.9 nm), see an asterisk.

*3.1.3. Frequency-Dependent Resonant Holes Obtained Using Constant Burning Fluence.* Figure 4A compares HB spectra excited at $\lambda_B$ = 820.81 nm (i.e., at the high-energy side of the 825 nm band (curve d)) and $\lambda_B$ = 496.5 nm (curve c) for intact FMO sample; its absorption spectrum (curve a) is shown for a comparison. Curve b is the absorption spectrum obtained after burning at $\lambda_B$ = 496.5 nm. Thus, curve c = b − a. The narrow and deepest hole in curve d (coincident with $\lambda_B$ = 820.81 nm) is referred to hereafter as the resonant hole, while the broad bleach within the 825 nm band is due to EET to the lowest energy exciton. The ZPH width at $\lambda_B$ = 820.81 nm ($\nu_B$ = 12 183.1 cm$^{-1}$) corrected for spectral resolution is 3.2 cm$^{-1}$ and corresponds to the EET time of ∼3.3 ps (see Figure 4B). Curve d also resolves two narrow vibrational holes at 36.5 and 75.1 cm$^{-1}$, which arise due to rapid vibrational relaxation in the excited state of a pigment followed by hole burning; these (pseudo-) vibrational satellite holes are marked with arrows. Typically, 36 and 70 cm$^{-1}$ modes were observed in fluorescence line-narrowed (FLN) spectra in ref 47, while 46 and 68 cm$^{-1}$ modes were also observed in delta FLN spectra obtained for *C. tepidum* FMO.[42] Note that these satellites holes are superimposed on a broad bleach with a minimum near 826 nm that is very similar to that obtained for NRHB, clearly indicating the presence of uncorrelated EET from higher-lying exciton states to the lowest energy exciton state of the trimer. We have shown before that the trimeric organization of FMO (with the same SDF for each BChl 3 mostly contributing to the 825 nm absorption band) leads to a triple splitting[48,49] (see Figure S1 of the Supporting Information (SI)).

To obtain more information on the excited-state lifetimes ($T_1$) and interexciton level relaxation, eight high-resolution (resonantly burned) ZPHs, burned in the spectral region of 810−821 nm (12180−12345 cm$^{-1}$) with a low constant fluence of 0.4 J/cm$^2$, are presented in Figure 4B. The shallow ZPH holes were also superimposed on a broad bleach (not shown) very similar to the bleach obtained with $\lambda_B$ = 820.81 nm (curve d in Figure 4A), which was subtracted. As mentioned above, such a broad spectral bleach is caused by excitonic relaxation followed by nonresonant burning of the lowest energy exciton state. Similar data were observed in WT *C. tepidum* FMO.[20,49] Solid black lines in Figure 4B are fitted Lorentzians plotted on top of the experimental (noisy) holes. The excited-state lifetimes that are related to the so-called homogeneously broadened lines, $\Gamma_{hom}$, where $\Gamma_{hom}$ = 1/2 $\Gamma_{ZPH}$,[50] can be obtained from eq 1

$$\frac{1}{T_2} = \pi c \Gamma_{hom} = \frac{1}{2T_1} + \frac{1}{T_2^*} \quad (1)$$

where $T_2$ is the total dephasing time and $T_2^*$ is the pure dephasing time that strongly depends on temperature since dephasing is caused by phonon scattering; c is the velocity of light (cm s$^{-1}$).[24] At $T$ = 5 K, $\Gamma_{hom}$ obtained for excitonically coupled systems are strongly dominated by the exciton level decay times ($T_1$), with $T_2^*$ being just a minor contribution.


https://dx.doi.org/10.1021/acsomega.1c00286
ACS Omega 2021, 6, 5990−6008

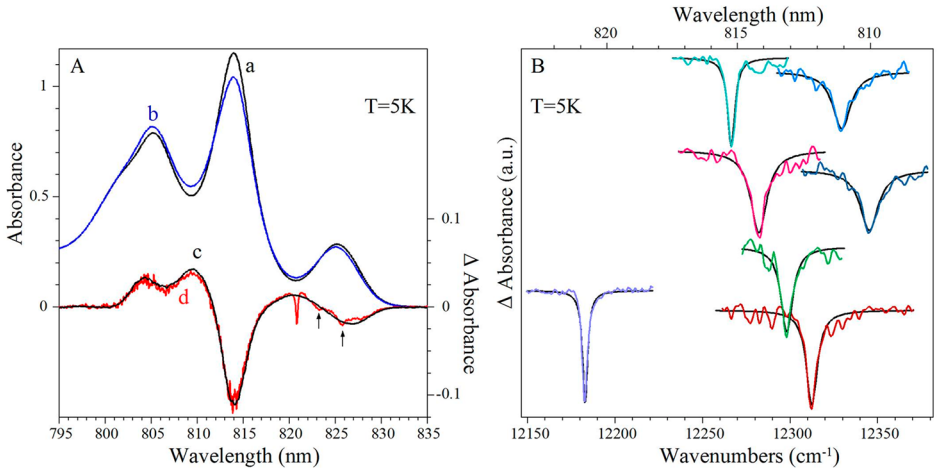


**Figure 4.** (A) Absorption spectrum (a) and HB spectra, curves c and d, obtained for our best FMO sample at $T$ = 5 K. Curves c and d are obtained with $\lambda_B$ of 496.5 nm (20 141 cm$^{-1}$) and 820.81 nm ($\nu_B$ = 12 183.1 cm$^{-1}$), respectively. Curve b is the absorption spectrum of the partly destabilized sample shown for comparison. Arrows mark satellite holes in curve d. (B) ZPHs obtained for *P. aestuarii* FMO at 5 K. Burning frequencies from left to right are: 12 183.1, 12 266.5, 12 281.4, 12 297.3, 12 311.7, 12 329.2, and 12 345.6 cm$^{-1}$, respectively. The ZPHs are fitted with single Lorentzian curves (solid black lines).

**Table 1. Frequency-Dependent $T_1$ Values in *P. aestuarii* ($T$ = 5 K)**

| ZPH position | | ZPH | | Resolution corrected | |
|---|---|---|---|---|---|
| (cm$^{-1}$) | (nm) | *fwhm* (cm$^{-1}$) | $T_1$ (ps) | *fwhm* (cm$^{-1}$) | $T_1$ (ps) |
| 12453.3 | 803 | - | - | - | 0.25 |
| 12437.8 | 804 | - | - | - | 0.5 |
| 12376.2 | 808 | - | - | - | 0.4 |
| 12345.6 | 810.0 | 11.83 | 0.90 | 11.45 | 0.93 |
| 12329.2 | 811.08 | 12.43 | 0.85 | 7.03 | 0.88 |
| 12322.9 | 811.5 | - | - | - | 1.55 |
| 12315.3 | 812 | - | - | - | 1.7 |
| 12311.7 | 812.24 | 7.59 | 1.40 | 7.03 | 1.51 |
| 12297.3 | 813.19 | 8.17 | 1.30 | 7.65 | 1.39 |
| 12281.4 | 814.24 | 11.25 | 0.94 | 10.87 | 0.98 |
| 12269.9 | 815 | - | - | - | 2 |
| 12266.5 | 815.23 | 5.11 | 2.08 | 4.28 | 2.48 |
| 12240.0 | 817 | - | - | - | 2.1 |
| 12187.7 | 820.5 | - | - | - | 3 |
| 12183.1 | 820.81 | 3.54 | 3.00 | 3.24 | 3.28 |
| 12150.7 | 823 | - | - | - | 4.95 |
| 12099.2 | 826.5 | - | - | - | 9.0 |
| 12062.7 | 829 | - | - | - | 9.5 |
| 12048.2 | 830 | - | - | - | 10.0 |

Therefore, $T_1 \sim (2\pi c\Gamma_{hom})^{-1}$.[24] As in the case of *C. tepidum* FMO and its several mutants, for low fluence no sharp holes could be burned at wavelengths shorter than ∼804 nm, indicating very fast relaxation times of high-energy excitons that decrease the quantum yield of the HB process.[51] The experimentally determined $T_1$ values based on the ZPHs, corrected for spectral resolution, are given in black in Table 1 and are further discussed in Section 4.5. For comparison, blue, pink, and green colors indicate values obtained by Franken et al.,[21] Louwe et al.,[52] and Vulto et al.,[36] respectively.

**3.2. Simulation of Optical Spectra, Population Dynamics, and Excition Lifetimes.** To provide insight into the excitonic structure and dynamics of the trimer, one needs to provide a properly parametrized (structure-based) Hamiltonian[8,9,13,20,44] that is consistent with various types of experimental data. As mentioned in the Introduction section, there have been several attempts to calculate[13,15−18] and/or extract (via simulations) the excitation (site) energies of BChls in various FMO complexes.[9−14] Several methods exist to calculate parameters such as electronic couplings between BChls,[52] optical transition energies of pigments in their protein binding site (site energies),[15,43] and spectral densities of pigment−protein couplings.[11,17] However, calculated site energies have to be further tuned using various algorithms to simultaneously describe multiple experimental data.[8,13,44] Our modeling studies discussed below show that even perfect fits of multiple spectra may not provide experimentally determined exciton lifetimes and/or expected exciton population dynamics.[36,38,53,54] Very recently Saito et al.,[17] using molecular dynamic (MD) simulations and a quantum mechanical/


https://dx.doi.org/10.1021/acsomega.1c00286
ACS Omega 2021, 6, 5990−6008

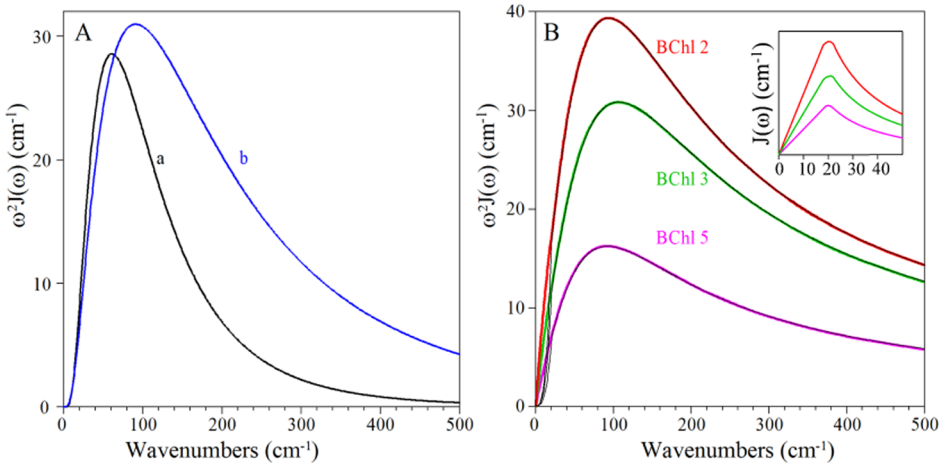


**Figure 5.** (A) Black (a) and blue (b) curves are lognormal spectral densities $J_1(\omega)$ for BChl 3 and $J_2(\omega)$ for BChls 1, 2, and 4−8. (B) Colored lines represent $C''(\omega)$ adopted directly from ref 17 for BChls 2, 3, and 5, respectively. The black curves (on top of colored ones) are $C''(\omega)$mod discussed in text for BChl 2, 3, and 5. The curves in the inset show respective modified $J(\omega)$ curves that are slightly smoothed at the maximum.

molecular mechanical (QM/MM) methodology, obtained individual site energies and spectral densities of BChls in *P. aestuarii* FMO complexes. These calculations revealed remarkably large site-energy fluctuations due to heterogeneity of the protein environment of individual BChls at both room temperature and 77 K.[17] Although their site energies described well the room-temperature absorption, they could not reproduce the shape of the 77 K absorption spectrum. Moreover, very recent calculations of Kim et al.,[18] using classical MD simulations for *C. tepidum* FMO, followed by the partial correction of pigment structures by constrained QM/MM geometry optimization (with effective fragments potential), also revealed large standard deviations ($\sigma$) for individual BChls in *P. aestuarii* FMO, varying from about 55 to 146 $cm^{-1}$ (i.e., with fwhm of 130−340 $cm^{-1}$). While the MD simulations reported in ref 18 were performed at room temperature, the same values were used to model their 77 K absorption and CD spectra. Importantly, similar $\sigma$-values (68−144 $cm^{-1}$, i.e., fwhm of 160−340 $cm^{-1}$) were obtained in ref 17. Therefore, it is crucial to test the influence of multiple spectral densities (and their shapes), as well as variable distributions (static disorder) of site energies, on the quality of fits of our optical spectra and resulting exciton lifetimes/population dynamics. Calculations are performed for FMO trimers with 21−24 BChls using the structure from the 3EOJ pdb file.[2]

*3.2.1. Phonon Spectral Densities.* In ref 41, we provided a critical assessment of typical phonon SDs, used to describe linear and nonlinear optical spectra in various photosynthetic complexes. For example, we have argued that the shapes of the overdamped Brownian oscillator (OBO, also called Drude−Lorentz) and Ohmic SDs, often used in the modeling of excitonic structure and dynamics of FMO complexes at cryogenic temperatures, are qualitatively wrong in comparison to the experiment, especially at very low frequencies.[41] Although the shape of the B777 SD often used in modeling studies, it can be used if its parameters are properly adjusted to fit experimental delta fluorescence line-narrowing (ΔFLN) spectra.[15,41,44] We have also shown the experimentally measured SDs of FMO;[8] the CP29 antenna complex of PSII,[55] CP47,[56] and WSCP[57] can be described using a lognormal distribution function. Moreover, often it is assumed that all pigments have the same shape of SD, but this does not have to be the case, as experimentally determined SDs (via ΔFLNS experiments) correspond only to pigment(s) largely contributing to the lowest energy exciton.

It is widely accepted that proper SD shapes are critical, as they describe the frequency-dependent coupling of the system to its bath.[58,59] SDs are also important components in calculations of EET times and exciton population dynamics.[60] Therefore, we also consider the recently calculated Drude−Lorentz SDs defined as $C''(\omega) = \omega^2 J(\omega)$, where $J(\omega)$ directly determines both spectral characteristics and exciton relaxation dynamics.[61] However, $J(\omega) = C''(\omega)/\omega^2$ extracted from Drude−Lorentz SD displays qualitatively wrong behavior when compared to the low-temperature phonon SD at zero frequency, where it should go to zero.[41] Therefore, all Drude−Lorentz SDs from ref 17, used in our modeling of 5 K optical spectra shown below, are slightly modified in the low-frequency region (≤20 $cm^{-1}$). The modification described below allows one to define the Huang−Rhys factor ($S$).[41]

$J_1(\omega)$ and $J_2(\omega)$, shown in Figure 5A (i.e., curves a (black) and b (blue), respectively) are the lognormal SDs used previously to model various optical spectra of *C. tepidum* FMO[8,20,33,62] (see the SI for details). Figure 5B shows the recently calculated Drude−Lorentz SDs for BChls 2, 3, and 5 (solid lines) from ref 17, compared with the corresponding modified shapes ($C''(\omega)$mod) in the low-frequency region (dashed lines) to eliminate divergence of the line shape function at zero frequency. The modification (see the SI for details) is made because the $S$-factor is the standard metric used to discuss electron−phonon coupling strength in HB spectroscopy (as opposed to reorganization energy used by theorists) and practically eliminates the low-frequency divergence. The remaining $C''(\omega)$mod for BChls 1, 4, and 6−8 are shown in Figure S2 in the SI. The $C''(\omega)$mod SDs for all BChls are referred to as SD1($\omega$), SD2($\omega$),..., SD8($\omega$). In Model I (Hamiltonian **I**; Table S1), we use $J_1(\omega)$ (obtained from the fit of the *C. tepidum* ΔFLN spectrum)[41] for BChl 3, while $J_2(\omega)$ is used for all remaining BChls.[8] In modeling, described below, we consider trimers with the variable number of pigments, i.e., 21−24 BChls. In Model II (Hamiltonian **II**; Table S2), we use the $C''(\omega)$mod Drude−Lorentz SDs.

Note that differences between $C''(\omega)$mod (dashed lines) and Drude−Lorentz SDs (solid lines), as illustrated in Figure 5B, are


https://dx.doi.org/10.1021/acsomega.1c00286
ACS Omega 2021, 6, 5990−6008

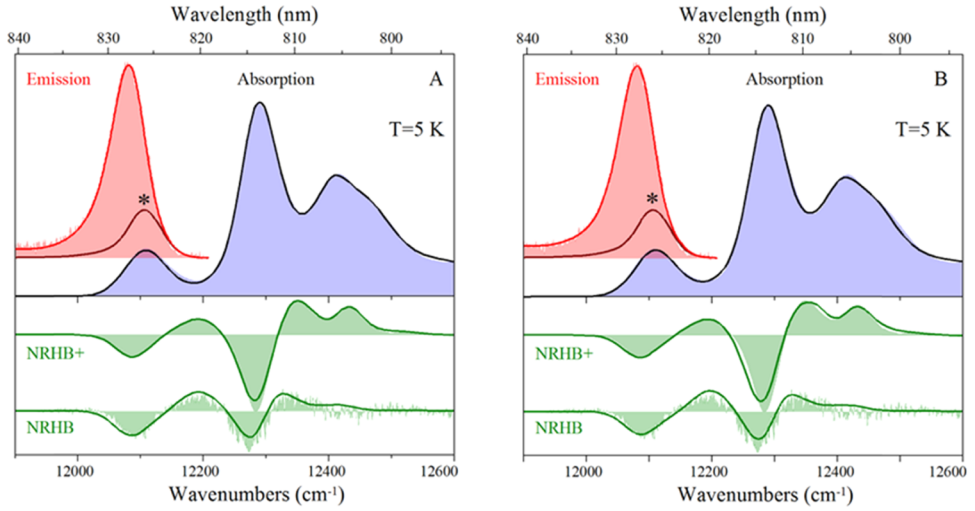


**Figure 6.** (A) Filled curves represent experimental data: absorption is blue, emission is pink, and HB spectra are green (see text for details for NRHB and NRHB+) at $T$ = 5 K. Solid lines are theoretical fits obtained with two spectral densities for 21 BChl per trimer (no BChls 8) with H **I** (see Table S1). (B) Same experimental data as in frame A with the exception that theoretical fits are obtained with seven modified Drude−Lorentz SDs (H **II**). Emission and HB spectra contain contribution from monomers (see text). The component marked with an asterisk represents the combined emission from the second and third exciton states. Theoretical curves are obtained for $10^6$ accumulations.

very small. Below we discuss in detail data obtained for Models I and II (with 21 BChls per trimer).

*3.2.2. Simultaneous Fits of Multiple Optical Spectra.* Filled spectra in Figure 6 are the experimental 5 K absorption (blue), emission (pink), and HB (green) spectra, obtained for our most intact *P. aestuarii* FMO (see Section 2 for experimental procedures). The 5 K emission spectrum was obtained with an excitation frequency of 20 490 $cm^{-1}$. Curve labeled NRHB+ is the nonresonant HB spectrum, i.e., subtracted absorption before and after nonresonant illumination at 20 490 $cm^{-1}$. Curve labeled NRHB is the red curve (f − d) from Figure 3. Curve NRHB can be fitted in the standard HB paradigm, where the pigments participating in the lowest exciton state can change their energy via tunneling in an electronically excited state. Parts of the curve labeled NRHB+, however, cannot be modeled in this paradigm—to explain the observed deep hole at ∼12 287 $cm^{-1}$ and positive HB signal at 12 435 $cm^{-1}$, one needs to let few other pigments (not participating in the lowest exciton state) to change energy in addition (and hence the + sign), vide infra. Solid curves in Figure 6 show the best-calculated spectra (absorption, black; emission, red; HB spectra, green). In this case, as before for *C. tepidum* FMO trimers,[8] we use $J_1(\omega)$ for BChl 3 and $J_2(\omega)$ for remaining pigments. That is, for BChl 3 (mostly contributing to the lowest energy exciton in FMO) we use a lognormal $J_1(\omega)$ (with $\omega_c$ = 38 $cm^{-1}$, $\sigma$ = 0.7) determined from experimentally measured ΔFLNS[42] for *C. tepidum* FMO.[41] For higher-energy pigments, we use a lognormal $J_2(\omega)$ (with $\omega_c$ = 45 $cm^{-1}$, $\sigma$ = 0.85).[8] At least two spectral densities were needed to model *C. tepidum* exciton dynamics and temperature-dependent spectra; the same is true for *P. aestuarii* FMO (data not shown). The parameters for $J_2(\omega)$ were determined from excitation-dependent FLN spectra of the B777 complex[63] (for a BChl *a* bound to a single α-helix protein). The S-factor in Model I (Hamiltonian (H)**I**, Figure 6A) was assumed to be site-independent. Very good fits of the absorption, emission, and regular NRHB spectra were obtained with the same Huang−Rhys factor ($S$ = 0.4).

Regarding the calculated spectra shown in Figure 6A (H **I**; see Table S1 for details), we note that the best simultaneous fit was obtained assuming 21 BChls per trimer and that ∼19% of emission likely originates from monomers that that did not transfer energy into the lowest-energy exciton state of the trimer (see band 1 in Figure S1). The calculated contribution to the measured emission spectrum from the monomer emission is indicated in Figure 6A,B as dark red curves labeled by asterisks. The best fits of HB spectra also allowed 19% of bleach to occur in monomers. No good fits were obtained assuming 22−24 BChls per trimer (data not shown); apparently, this sample (as all other *P. aestuarii* samples studied in this laboratory) does not contain any BChl 8. In the fits shown in Figure 6B (for H **II**; see Table S2), modified Drude−Lorentz SDs were used in calculations. Calculated S-factors are: SD1 ($S$ = 0.49), SD2 ($S$ = 1.66), SD3 ($S$ = 0.5), SD4 ($S$ = 0.36), SD5 ($S$ = 1.21), SD6 ($S$ = 0.41), and SD7 ($S$ = 0.51). In this case, the emission spectrum also contains 19% contribution from FMO monomers, while 81% originates from the lowest exciton of the FMO trimer (band 1 in Figure S1). The same is true for the HB spectra, that is, 19% bleach within the 825 nm band originates from the monomers (see Figure S3 in the SI). BChl 1−7 contributions ($d_m(\omega)$) to the calculated absorption spectra shown in Figure 6A,B are shown in frames A and B, respectively, of Figure S4 in the SI. Seven exciton states (and their averaged energies) calculated for *P. aestuarii* monomer based on the optical spectra fitted in Figure 6A (two SDs; H **I**) and 6B (seven SDs; H **II**) are shown in Figure S5 in the Supporting Information. Wavelength-dependent distributions of exciton lifetimes for the last two Hamiltonians are illustrated in Figure S6.

Although the analysis of the spectra shown above suggests that *P. aestuarii* FMO samples studied in our laboratory contained 21 BChls per trimer, the latter does not mean that BChls 8 are always lost in FMO complexes. In fact, as shown in the SI, good fits of optical spectra adopted from ref 12 were obtained assuming 24 BChl per trimer. However, these spectra were digitized from old papers so there may be small spectral shifts in digitized spectra. Thus, the fits shown in Figure S7 are only shown for comparison. Hamiltonians **III** (with two SDs) and **IV** (with eight modified Drude−Lorentz SDs) and Tables S7 and S8 are briefly discussed in the SI. Here, we only note that fits of


https://dx.doi.org/10.1021/acsomega.1c00286
ACS Omega 2021, 6, 5990−6008

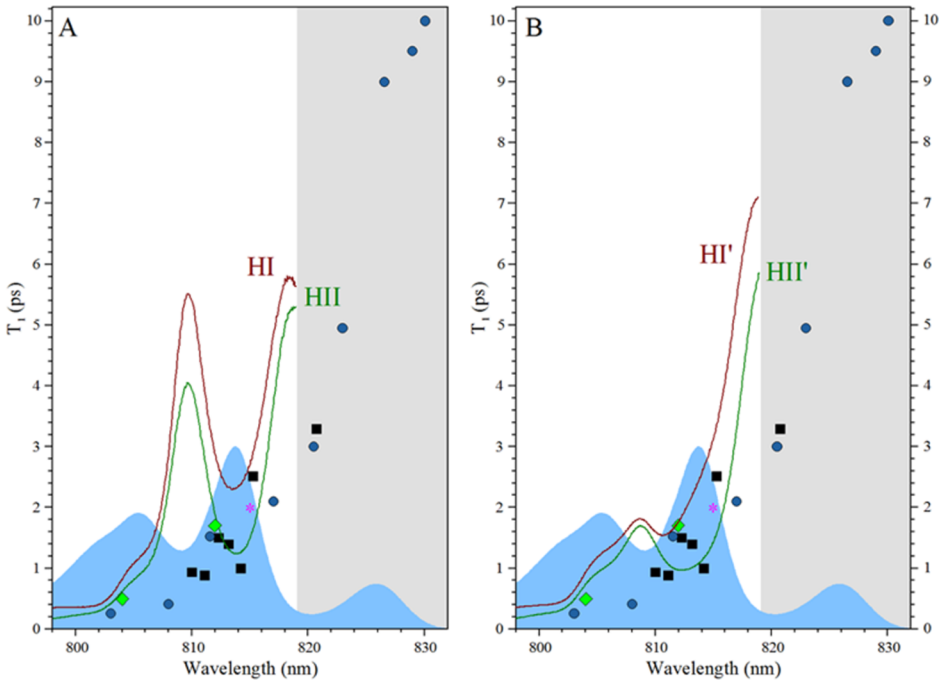


**Figure 7.** Black squares in both frames correspond to the excited-state decay times ($T_1$) calculated from the resonant (resolution corrected) holes (shown in Figure 4A,B) as a function of $\lambda_B$. Blue circles are $T_1$ times calculated based on $T_2$ times obtained from HB data reported in ref 21. Green diamonds are $T_1$ from 10 K time-resolved absorption measurements.[36] The pink asterisk is the 2 ps $T_1$ time from accumulated photon echo measurements.[64] Brown/green curves in frames A and B show averaged $T_1$ values for H **I**/H **II** and H **I′**/H **II′**, respectively. Filled blue curves show the 5 K FMO absorption spectra for comparison.

Vulto et al. data suggest that BChl 8 contributes near 805 nm in agreement with previously published experimental and modeling data obtained for *C. tepidum* FMO.[8,18,35] Interestingly, the site energy of BChl 8 revealed by our modeling is in good agreement with the calculated value reported in ref 18, though it is at much lower energy than that calculated in ref 17. Nevertheless, it is likely that some samples may contain eight BChls per monomer. Several other models with different combinations of SDs (and partial occupation of BChl 8) were also tested; however, none of them provided good fits of our spectra (data not shown for brevity).

*3.2.3. Experimentally Determined and Calculated Wavelength-Dependent Exciton Lifetimes.* The black squares in Figure 7 are obtained from the $\Gamma_{ZPH}$ at different burn wavelengths ($\lambda_B$) shown in Figure 4B. Recall that the fwhm of the resonant holes ($\Gamma_{ZPH}$) shown in Figure 4B depend on the burning frequency and reveal frequency-dependent exciton lifetimes. The blue circles were previously obtained from HB data,[21] though at larger burning fluence compared to this work (96 versus 0.4 J/cm$^2$). Lower fluences minimize saturation and fluence broadening, so it is possible that the $T_1$ values represented by the blue circles could be somewhat larger. The green diamonds and pink asterisk correspond to $T_1$ times obtained by pump-probe[36] and 2D photon echo spectra,[64] respectively. The filled blue curve is the absorption spectrum shown for an easy comparison. As in other FMO complexes (including various FMO mutants), at low fluence, no well-resolved holes were bleached at wavelengths shorter than ~803−804 nm,[20,51] indicating that the lifetimes of the exciton states in this spectral region are too short for HB to be observed. That is, in such a case very fast EET removes the excitation from a given exciton and reduces the probability of nonphotochemical HB (NPHB).[24] This behavior was also observed in several FMO mutants from *C. tepidum*, each showing a different wavelength dependence of $T_1$.[33]

Figure 7A compares calculated (averaged) exciton lifetimes obtained with H **I** (brown curve) and H **II** (green curve) with experimentally determined $T_1$ values from different types of experiments mentioned above. The brown and green curves in Figure 7B are obtained with H **I′** and H **II′**, respectively. We emphasize that the calculated curves are obtained for FMO trimers while neglecting the three lowest energy exciton states (see Figure S1 in the Supporting Information). This is because in the ~819−830 nm region one would have to consider simultaneously a non-Markovian reduced density matrix theory[44] and the uncorrelated disorder-averaged Förster EET time between FMO monomers using generalized Förster theory.[65] This has not been done as yet; thus, the discrepancy between the calculated and experimental data in the spectral region about 819−830 nm was anticipated. Nevertheless, based on the width of the ZPHs (burned in *P. aestuarii* within the 810−818 nm spectral range), we conclude that the experimentally determined excited-state lifetimes vary from about 0.7−2.5 ps (see Table 1 for details).

Comparison of the averaged $T_1$ values for H **I** (brown curve) and H **II** (green) with experimentally determined $T_1$ values in Figure 7A clearly indicates that calculated maxima near 810 nm are inconsistent with the experimental data, although simultaneous fits of various optical spectra shown in Figure 6 are very good. Extensive modeling studies using our fitting algorithm could not eliminate the 810 nm maximum in Figure 7A by changing BChl site energies and/or inhomogeneous broadenings. Note that different shapes of phonon spectral densities used to obtain H **I** and H **II** weakly affect the general shape of averaged $T_1$ distributions, i.e., in both cases, there is a maximum near 810 nm. However, the TrEsp calculated coupling matrix


https://dx.doi.org/10.1021/acsomega.1c00286
ACS Omega 2021, 6, 5990−6008

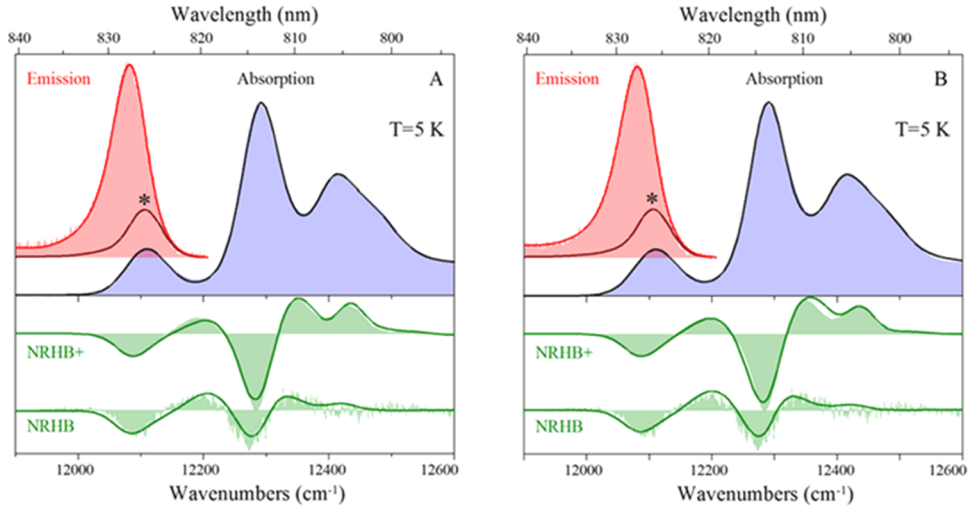


**Figure 8.** Filled curves in both frames are the same experimental spectra as those shown in Figure 6. Solid lines are theoretical fits obtained with modified Hamiltonians H **I**′ (frame A) and H **II**′ (frame B). Theoretical curves are obtained with slightly modified $V_{1,4}$, $V_{2,4}$, $V_{7,1}$, and $V_{6,2}$ couplings.

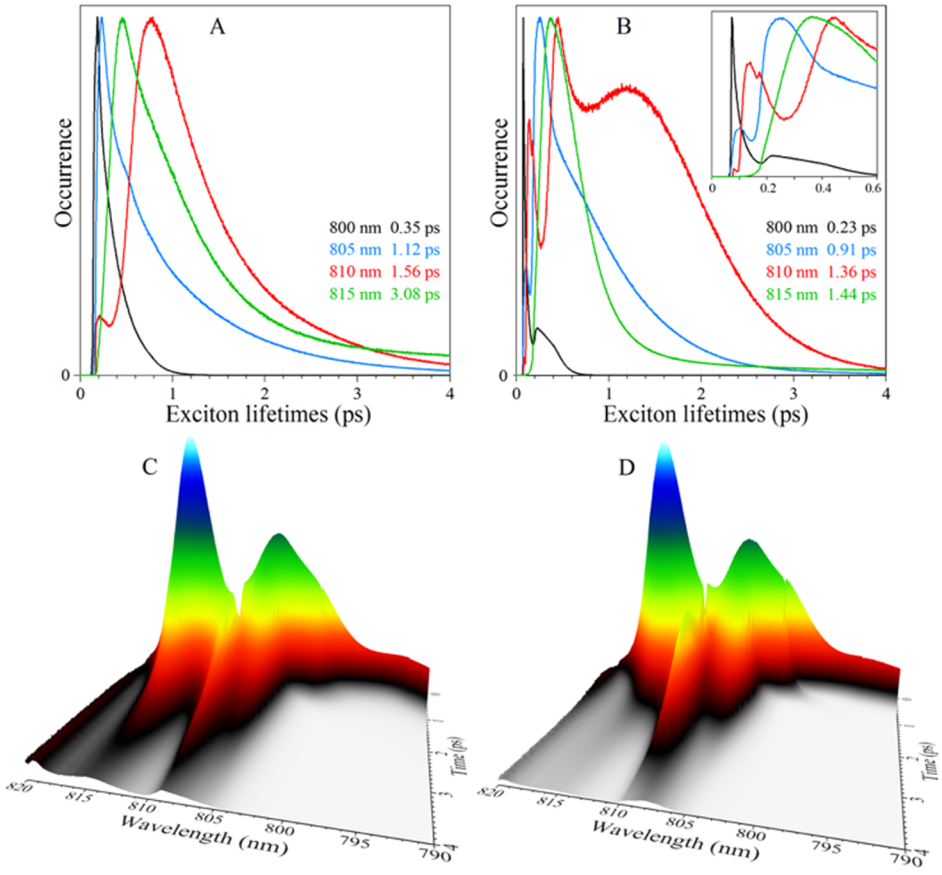


**Figure 9.** Wavelength-dependent distributions of exciton lifetimes (averaged over ±0.5 nm for $50 \times 10^6$ complexes with normalized amplitudes) at 800 (black), 805 (blue), 810 (red), and 815 ± 0.5 nm (green) using H **I**′ (frame A) H **II**′ (frame B). *Average* exciton lifetimes (ps) are indicated with color-coded numbers. Corresponding full 3D distributions plotted versus wavelength and time are shown in frames (C) and (D), respectively. These distributions were obtained for $10^8$ accumulations for a FMO monomer. Distributions are calculated with a step of 0.25 nm. Distributions in top panels are *normalized* to the same value; individual distribution amplitudes in bottom panels are normalized to the absorption at the respective wavelength.

elements ($V_{n,m}$) do not have to be perfect and their values (and/or possible distributions) can also affect exciton dynamics. Indeed, we found that the maximum in $T_1$ values near 810 nm (see Figure 7A) is very sensitive to several coupling constants. For example, changing $V_{1,4}/V_{2,4}/V_{7,1}$ by only −5 $cm^{-1}$ and $V_{6,2}$ by +5 $cm^{-1}$ significantly decreases the maximum near 810 nm. This is illustrated in Figure 7B where the brown and green curves are calculated using H **I**′ (brown curve) and H **II**′ (green curve) with slightly modified $V_{1,4}$, $V_{2,4}$, $V_{7,1}$, and $V_{6,2}$ parameters. Thus, we conclude that the calculated 2−5 ps $T_1$ values in the 808−812 nm region (see Figure 7A) are not real, as clearly indicated by the data points from the frequency- and time-domain


https://dx.doi.org/10.1021/acsomega.1c00286
ACS Omega 2021, 6, 5990−6008

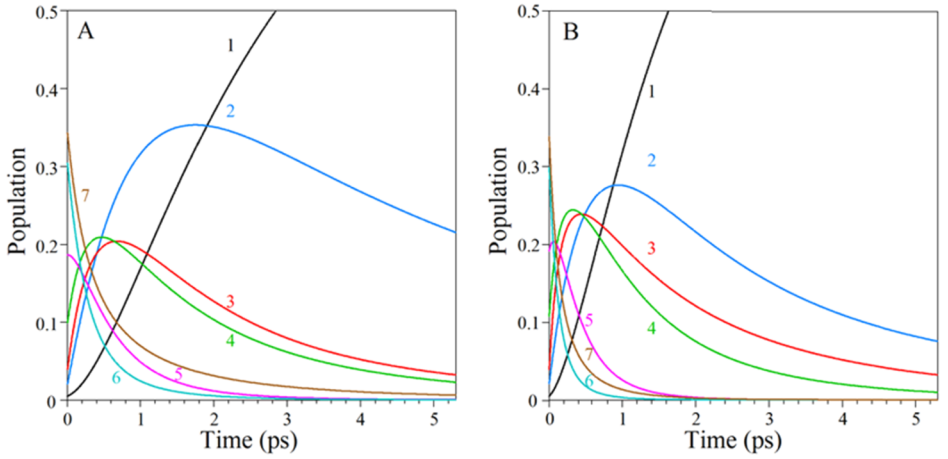


**Figure 10.** Exciton population dynamics at $T = 5$ K after initial excitation by a 50 fs laser pulse at 12 626 $cm^{-1}$. The total population is 1. Frames (A) and (B) are obtained for H **I**′ and H **II**′, respectively.

experiments. This modification led to slightly modified site energies and site-dependent inhomogeneities as illustrated in Figures 12B and 13B. We hasten to add that H **I**′ and H **II**′ also provide very good fits of our optical spectra (see Figure 8). We focus below on the excitonic structure and dynamics described by H **I**′ and H **II**′ as they provide better agreement with experimental data. A small modification of coupling constants in H **I**′ and H **II**′ is justified as in the TrEsp methodology; there is uncertainty concerning calculated transition densities (and, therefore, partial charges) and ambiguity regarding the influence of the polarizability of the dielectric environment.[66]

*3.2.4. Frequency-Dependent Exciton Lifetimes and Their Distributions.* Frames A and B in Figure 9 show wavelength-dependent distributions (with normalized amplitudes) of exciton lifetimes averaged over ±0.5 nm at 800 (black), 805 (blue), 810 (red), and 815 nm (green) using H **I**′ (A) and H **II**′ (B), respectively. Note that at these wavelengths it is enough to use a non-Markovian reduced density matrix. Color-coded average lifetimes for each curve are listed in the lower right corners; the inset in frame B shows expanded distribution onsets for H **II**′. The distribution shapes depend strongly on wavelength. For example, H **II**′ (obtained with *seven* SDs; Figure 9B) reveals several wavelength-dependent maxima. For example, at 810 nm, the maxima are at 80, 136, 180, and 440 fs in agreement with 2DES experiments.[37,60] At 800 nm, the maxima are at about 70 and 220 fs, while at 805 nm, the maxima are near 100 and 250 fs. Rapid decaying electronic quantum coherence on the time scale of 60 fs was also observed in *C. tepidum* FMO.[67] For H **I**′ at 800 and 805 nm, the maximum are at 190 and 230 fs. At 810 nm, there are two peaks at 220 and 770 fs, while at 815 nm, the peak is located near 460 fs. Full three-dimensional (3D) distributions of averaged exciton lifetimes (plotted versus wavelength and time) are shown in frames C and D for H **I**′ and H **II**′, respectively, see Section 5.5 for more details.

*3.2.5. Calculated Population Dynamics.* The resulting population dynamics for our best Hamiltonians (H **I**′ and H **II**′; see Tables S1, S2, S13, and S15) calculated for a monomer containing seven BChls are plotted in Figure 10A,B, respectively. In both cases, the initial populations are calculated assuming excitation by a 50 fs laser pulse at 12 626 $cm^{-1}$ as in ref 60. Data shown in frames A and B are obtained with *two* and *seven* SDs as discussed above. Note that for stronger electron−phonon couplings and seven SDs (frame B) the exciton population dynamics is faster than that shown in frames A for two SDs. In both cases, however, states 5, 6, and 7 have the largest initial populations, with the lowest energy state 1 having a negligible initial population. By 5 ps, the population of state 1, in frames A and B, is approximately 72 and 88%, respectively. Note very fast decaying dynamics of high-energy states is observed in the first 500 fs. For H **I**′ (frame A) and H **II**′ (frame B), exciton 2 decays slowly. The population dynamics is strongly dependent on the assumed shape of phonon spectral densities (see Figure 10A,B) as well as the interpigment coupling (data not shown).

Similar dynamics was obtained with Hamiltonians **III** and **IV** fitting spectra from ref 12 (see Figure S9 in the SI). Interestingly, Hamiltonians **II**′ and **IV** (both calculated with seven and eight site-dependent SDs, respectively) accelerate overall population dynamics. Note that exciton state 3 (calculated with H **II**′) decays faster than exciton 2. Similar behavior was observed in Hamiltonian **IV**, probably due to better overlap with exciton 1. In addition, the EET time from BChl 8 (placed in a separate domain) to the adjacent monomer, using generalized Förster theory, is about 7 ps.

## 4. DISCUSSION

**4.1. 5 K Absorption, Emission, and NRHB Spectra.** Small differences between absorption spectra a and b in Figure 2A are likely caused by different preparation/purification and/or storage procedures. However, the differences between HB spectra (curves c and d), in particular different hole depths near 814 nm, are most likely caused by sample-dependent protein conformational changes during the nonphotochemical HB process. Since the small shifts of the absorption spectra are sample-dependent and blue shifts are more visible in purposely aged samples, we suggest that both curves a and b in Figure 2A could be mixtures with different ratios of intact to partly destabilized complexes. However, it is difficult to estimate a contribution from destabilized complexes since their contribution varies from sample to sample (data not shown) affecting the shape of HB spectra, especially the hole depth near 814 nm (12 287 $cm^{-1}$) and the positive band near 804 nm (12 435 $cm^{-1}$) (see hole burned curves in Figure 6A/B). A simple scaling/subtraction method suggests that even our best sample (characterized by curves b and c in Figure 2A) could contain about 20% of partly destabilized complexes.

Recall that the ratios of the two lowest energy bleaches in spectra c and d in Figure 2A are very different from the ratio


https://dx.doi.org/10.1021/acsomega.1c00286
ACS Omega 2021, 6, 5990−6008

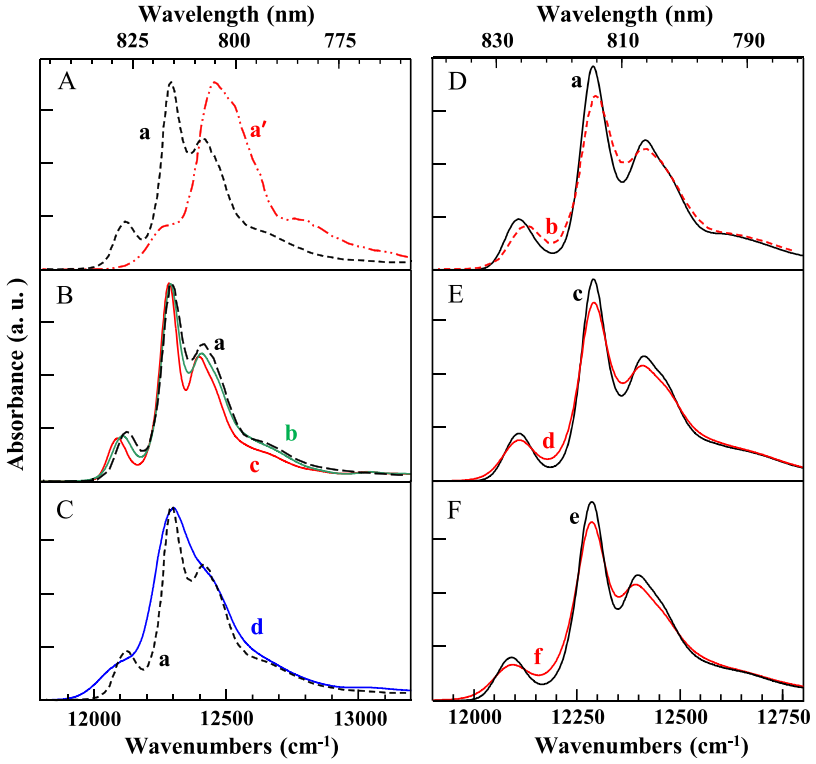


**Figure 11.** Curves a in frames A−C (dashed lines) are the experimental 77 K absorption spectra of *P. aestuarii* adopted from refs 2 and 68. Curve a′ in frame (A) is the calculated 77 K spectrum with seven modified Drude−Lorentz type SDs based on ref 17. Curves b and c in frame (B) are the calculated 77 K spectra using our site energies and $\Gamma_{inh}$ listed in H **I** (two SDs) and H **II** (seven SDs), respectively. (For *S*-values used to calculate curves b and c, see text.) Spectrum d in frame (C) is 77 K absorption calculated with site energies listed in H **II**, seven modified SDs, and $\Gamma_{inh}$ reported in ref 17 Curves a and b in frame (D) are the experimental absorption spectra obtained at 5 K (this work) and 77 K,[25] respectively. Curves c and d in frame E are calculated absorption spectra at 5 and 77 K, respectively, using site energies and $\Gamma_{inh}$ from H **I** with two SDs. Curves e (5 K) and f (77 K) in frame F are obtained with parameters of H **II** (i.e., using seven (modified) Drude−Lorentz SDs and corresponding *S*-values listed in text).

observed in the extracted HB spectrum (f − d) shown in Figure 3. In Figures 6A and 8A, these curves are referred to as regular NRHB since they can be described theoretically assuming that only BChls 3 and 4 (contributing to the lowest energy state) are bleached, in agreement with the standard HB theory[24] (in H **I**/H **I**′ BChls 3 and 4 contribute to the lowest energy exciton 90.3/90.3 and 8.6/8.4%, respectively). The same contributions in H **II**/H **II**′ are 89/89 and 10/10%, respectively. The best fits of NRHB in Figures 6A/8A (with two SDs; H **I**/H **I**′) were obtained shifting BChls 3 and 4 blue by 97/117 and 104/104 $cm^{-1}$, respectively, on the protein configurational energy space upon burning, while for the best fits in Figures 6B/8B (with seven SDs; H **II**/ H **II**′), the same BChls had to be shifted blue by 104/106 and 127/133 $cm^{-1}$, respectively. However, good fits to the NRHB+ spectra in Figures 6A/B and 8A/B (solid green lines) could be obtained only when, in addition to the lowest energy pigments, other pigments (i.e., BChl 4 and BChl 6) were also allowed to change energy. For example, in the fits of NRHB + spectrum in Figures 6A/8A, about 38/37% of BChl 4 and 34/28% of BChl 6 change their site energy by 104/127 and 17/24 $cm^{-1}$, even when not selected as the burned pigment by the standard HB algorithm (see Section 2.3). Pigment inhomogeneities in H **I**/H **I**′ were nearly identical, while in H **II**/H **II**′, they only slightly changed for BChls 1, 2, 4, and 7 by −13, 7, 5, and −4 $cm^{-1}$, respectively. Thus, the modeling study suggests that the additional bleach of BChls 4 is responsible for the increased hole depth near 814 nm (peaking at 12 287 $cm^{-1}$) and positive product signal between 12 320 and 12 480 $cm^{-1}$ in the NRHB+ spectrum. The small shift of the BChl 6 on the energy landscape provides the product signal around near 804 nm, i.e., the second positive bump near 12 435 $cm^{-1}$.

Since the ∼825 nm bands in spectra a and b in Figure 2A are slightly shifted, also the emission spectra originating from their lowest energy states should be shifted and may have somewhat different shapes. This is indeed observed in Figure 2B where spectrum a (measured on a more destabilized sample) is broader and blue-shifted in comparison with spectrum b obtained for the more intact FMO. Curve c is the difference between spectra a and b, which we assign mostly to the emission from partly destabilized complexes. However, analysis of multiple spectra (in agreement with modeling studies; vide infra) suggests that both emission spectra (curves a and b) possess some contribution from monomer emission due to imperfect EET between monomers in a particular FMO trimer. The shape of curve c (Figure 2B) suggests that emission represented by curve a has a larger contribution from second and third lowest energy excitonic states of the trimer, in agreement with calculated spectra shown in Figure 6A/B. Thus, a weak contribution from monomer emission (∼19%) is observed due to imperfect EET between 3 → 2, 2 → 1, and 3 → 1 exciton states within the lowest energy 825 nm absorption band. (Three lowest energy exciton states calculated for *P. aestuarii* using H **I** and H **II** are plotted in Figure S1 in the Supporting Information.) Although emission in trimers with efficient EET between monomers originates mostly from substate 1, calculations show that at 5 K for all four Hamiltonians (H **I**/H **I**′ and H **II**/H **II**′), there is a small probability that about 4% of emission may still originate from the second and third excitons of the trimer.


https://dx.doi.org/10.1021/acsomega.1c00286
*ACS Omega* 2021, 6, 5990−6008

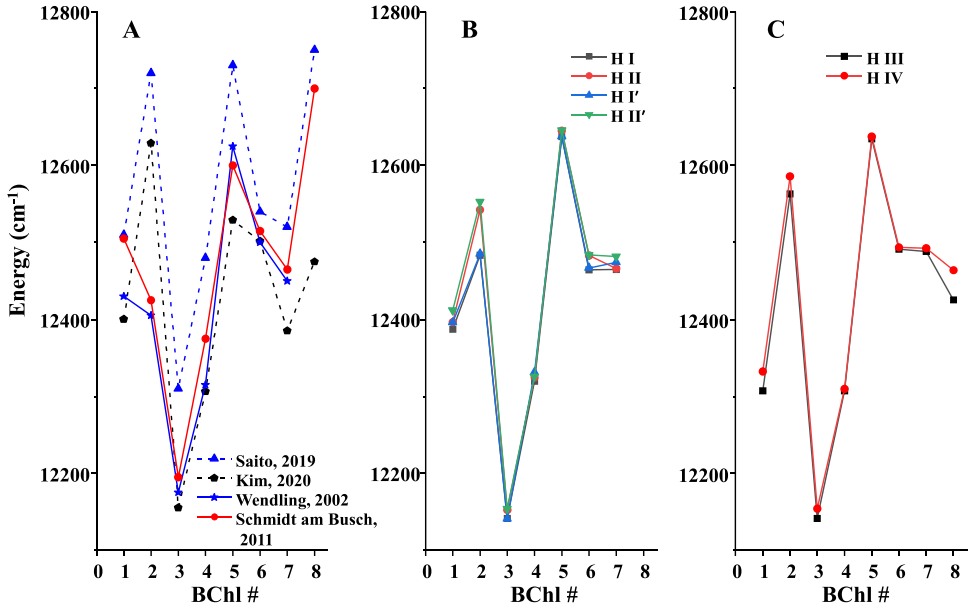


**Figure 12.** (A) Comparison of the recently calculated site energies[17,18] with values obtained from modeling studies reported in refs 9 and 25. Blue triangles and black pentagons are calculated site energies in refs 17 and 18, respectively. Red circles and blue squares are simulation extracted site energies from refs 9 and 25, respectively. (B) Comparison of site energies from H **I**/H **I′** and H **II**/H **II′** (this work, see Table S13) obtained from a simultaneous fit of experimental spectra shown in Figures 6A/8A and 6B/8B, respectively. Recall that for H **I**/H **I′** and H **III**, two SDs were used, while H **II**/ H **II′** and H **IV** were obtained with seven and eight SDs, respectively. (C) Site energies obtained for Hamiltonians H **III** and H **IV** (for details, see Figures S7A/S7B and Tables S13/S15 in the Supporting Information).

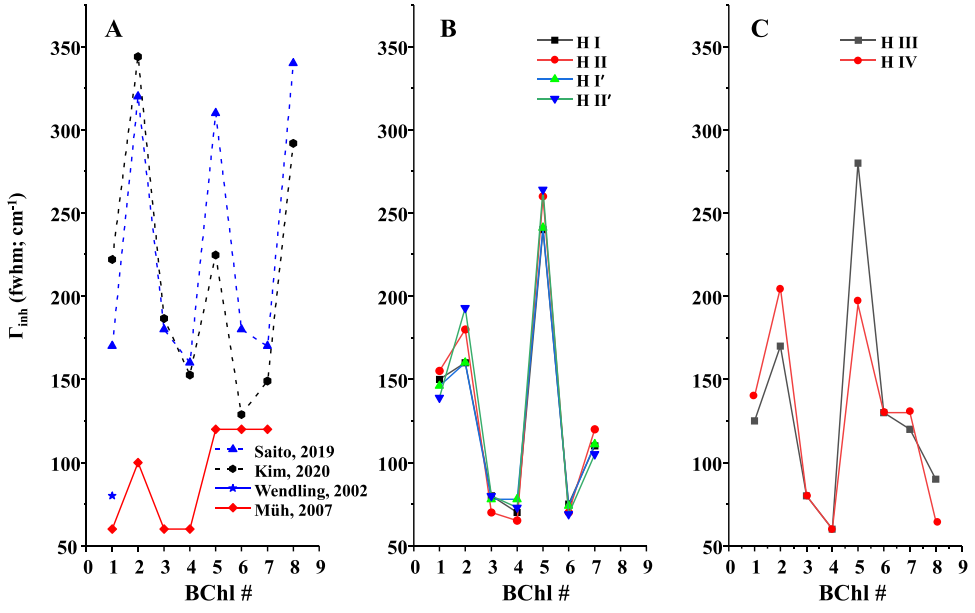


**Figure 13.** (A) Top two sets of data (blue triangles and yellow diamonds connected by dashed lines) are calculated (via MD simulations) $\Gamma_{inh}$ values for *P. aestuarii* reported in refs 17 and 18, respectively. Black squares below correspond to $\Gamma_{inh}$ from ref 15 ($\Gamma_{inh}$ values were not mentioned in ref 9). The blue asterisk indicates fixed $\Gamma_{inh}$ value of 80 cm$^{-1}$ used to fit spectra reported in ref 25. (B) $\Gamma_{inh}$ values obtained from the modeling of spectra shown in Figures 6A/8A (H **I**/H **I′**) and Figures 6B/8B (H **II**/H **II′**). (C) $\Gamma_{inh}$ values obtained for H **III** and H **IV** (fitted spectra are shown in Figures S7A and S7B, respectively).

**4.2. Hole-Burned (HB) Spectra Burned at $\nu_B$ = 12 284 cm$^{-1}$.** As mentioned above, FMO samples might be a mixture of intact and destabilized (minor contribution) proteins and EET between monomers could be absent in a fraction of complexes. Moreover, if there is a broad distribution of EET rates, HB may occur in some monomers before EET between monomer takes place. Furthermore, we cannot exclude that during the HB process in destabilized proteins pigments other than those contributing to the lowest energy exciton may tunnel on the energy landscape of the protein. That is, if significant nonradiative decay processes occur, the energy deposited into the nuclear motion of the pigment−protein complex could lead to small protein conformational changes, rearranging some pigments on the relatively smooth energy landscape.

The complex structure of the nonresonant holes shown in Figure 3 suggests that the NPHB mechanism in *P. aestuarii* varies


https://dx.doi.org/10.1021/acsomega.1c00286
ACS Omega 2021, 6, 5990−6008

from that observed in *C. tepidum* FMO,[20,34,48] and two different burning mechanisms likely contribute to the nonresonant holes shown in Figure 3. We propose that the deeper bleach near 814 nm is contributed to by tunneling of chromophore(s) not contributing to the lowest energy exciton in a fraction of complexes. This possibility was tested by the modeling study. That is, we showed that only the bleach represented by the red curve (f − d) in Figure 3 results from a regular NRHB process, where only pigments contributing to the lowest energy state are bleached (i.e., randomly shifted to different energies via tunneling on the protein energy landscape) as predicted by the standard HB theory[24,50] and observed for *C. tepidum* FMO. Moreover, we showed that the nature of additional bleaches (if present) could be exposed by our fitting algorithm. In fact, it was already suggested in ref 21 that some of the broad spectral changes observed in *P. aestuarii* FMO can be induced by protein conformational change, though its nature and/or theoretical description was not provided at that time. If a resonant hole is burned into the center of the 814 nm band, two processes compete—resonant hole burning at $\nu_B$ and fast EET to the lowest state, followed by energy changes of the lowest energy pigments (BChls 3 and 4) due to NRHB. The latter creates broad and featureless changes in the spectrum on top of which appears a weak resonant ZPH.

**4.3. Temperature Dependence of Absorption Spectra—Effect of Different Shapes of Spectral Densities.** Curves a in frames (A−C) of Figure 11 (dashed lines) are the experimental 77 K absorption spectra of *P. aestuarii* FMO adopted from refs 2, 25, and 68. Spectrum a′ in frame A is the calculated 77 K absorption spectrum of *P. aestuarii* (with seven modified Drude−Lorentz SDs and site energies and site-dependent $\Gamma_{inh}$ from ref 17). Curve a′ is nearly identical as the calculated 77 K absorption with Drude−Lorentz SDs in ref 17. Curves b and c in frame B are the calculated 77 K absorption spectra (no optimization) using the site energies, $\Gamma_{inh}$, and S-factors used to calculate 5 K spectra shown in frames A and B of Figure 6, respectively. Spectrum d in Figure 11C is 77 K absorption calculated with our site energies listed in H **II**, seven modified SDs, but $\Gamma_{inh}$ calculated by Saito et al.[17] showing that these $\Gamma_{inh}$ values are overestimated and poorly describe 77 K (or 5 K, not shown) absorption spectra. That the calculated room-temperature disorder is significantly larger is not surprising since as temperature increases so does the energy disorder. However, as demonstrated below, the trend in site energies and extent of site-dependent disorder is in very good agreement with our modeling studies (see Figures 12 and 13).

Spectra a and b in Figure 11D are the experimental absorption spectra obtained at 5 K (this work) and 77 K from ref 2. The slightly shifted spectrum b must correspond to a partly destabilized sample, as indicated by small shifts of the 825 nm band; nevertheless, the temperature effect is clearly visible and can be compared with our calculated 5 and 77 K spectra, i.e., curves c/d and e/f shown in frames E and F, respectively. Spectra c/d and e/f were calculated using H **I** and H **II**, respectively. The above analysis also holds for calculated spectra using H **I**′ and H **II**′ (data not shown). It appears that both sets of SDs describe well the weak temperature dependence of absorption spectra, suggesting that the shapes of SDs itself cannot differentiate which set of parameters best describes the excitonic structure of the *P. aestuarii* complex. Recall that all four Hamiltonians describe data shown in Figures 6A/B and 8A/B very well with only slightly modified sets of site energies and inhomogeneities (see Tables S13/S15 and Figures 12B/13B). The latter is not surprising since the utilization of different SDs and small changes in coupling constants required an adjustment of site energies and site-dependent inhomogeneities, i.e., these parameters are partly interdependent.

**4.4. Possible Mechanisms for NRHB+ Burning.** In the standard theory of NRHB processes, only a single pigment contributing to the lowest energy state changes energy. It is because of the assumption that excitonic and vibrational relaxation are so fast that the amount of "hot" HB is insignificant. To fit the NRHB+ spectra (see Figures 6A/B and 8A/B), it was necessary to assume that other pigments (than the ones, which contribute to the lowest energy state) can also change energy due to nonresonant excitation. The modified algorithm to calculate HB spectra in this case is as follows: First, the algorithm checks whether a particular pigment contributes to the lowest energy state; if yes, then its site energy is allowed to change (the regular NRHB process). That is, any pigment can burn regardless of its site energy, but the probability to do so is proportional to pigment's thermal occupation number when it is also contributing to the lowest exciton state. Second, if the particular pigment does not contribute to the lowest energy exciton, its site energy can also be changed with some probability. Whether the pigment has the lowest energy or not, the photoproduct site-energy values are taken randomly from the same SDF. If all probabilities are zero, NRHB+ will be identical to the regular NRHB. Pre- and postburn pigment energies in our density matrix approach are uncorrelated, i.e., they are randomly picked from two independent Gaussian SDFs.

The mechanism for NRHB+ could arise from a non-photochemical HB mechanism, where the amorphous medium (protein scaffolding) around the chromophore reorganizes in response to perturbation caused by the electronically excited state, allowing the chromophore to tunnel. After the chromophore relaxes to the ground state, the chromophore has a different energy. The energy change of a chromophore is caused by conformational changes in its environment. It is entirely possible that the rearrangement around the lowest energy pigment induced changes in the scaffolding around few other pigments. Due to the random nature of chromophore scaffolding, some configurations are more stable than others and, thus, there is a finite less-than-one probability that some other pigments may also undergo tunneling.

Another NRHB+ mechanism is also possible. Calculations show that (independent of Hamiltonian tested) BChl 3 contributes about 90% to the lowest energy exciton. Assume that its HB quantum yield ($\phi_{HB}$) is very low, i.e., the protein scaffolding around this chromophore is very rigid. If $\phi_{HB}$ of BChls 4 and 6 are significantly higher (due to favorable energy landscapes around these pigments), all three pigments may participate in the HB process in close proportions. In NRHB, the photosystem is excited at very high energy from where it relaxes to the lowest energy state. That is, the higher-energy pigments stay excited for a few picoseconds and relax to the lowest state that stays excited for a few nanoseconds. In most photosynthetic systems, the lowest pigment's HB contribution is therefore about 1000 times more efficient than HB from the intermediate (i.e., "hot" states). However, in systems where the lowest state hardly burns, the "hot" states HB may become observable. This mechanism would then be an analogue to the hot luminescence, i.e., hot HB. This would not change the emission's nature, as it still occurs from the lowest exciton state with the same lifetime and it still competes with the regular NRHB from the lowest state. We hasten to add that the NRHB+ mechanism was


https://dx.doi.org/10.1021/acsomega.1c00286
*ACS Omega* 2021, 6, 5990−6008

introduced only because the experimental spectrum could not be explained by pure excitonic effects as observed in *C. tepidum* FMO[8] and CP43/CP47 photosynthetic antenna complexes,[69] where we demonstrated that the NPHB spectra are dominated by the statistical reshuffling of site energies and by altered excitonic transition energies of both excitonic states (in contrast with only the lowest state). That is, although shifting the site energies of FMO pigments contributing to the lowest energy exciton also produces changes in the higher-exciton levels, the latter effect by itself could not explain the large bleach near 814 nm (see Figure 6A/B).

**4.5. Experimentally Determined and Calculated Wavelength-Dependent Exciton Lifetimes.** As shown above, the calculated $T_1$ values for H **I** and H **II** are inconsistent with the experimental HB and time-domain data near the 810 nm spectral region. Much better agreement is obtained using Hamiltonians H **I**′ and H **II**′. The calculated decay from the higher-energy exciton state(s) occurs on a sub-picosecond time scale and is very short at $\lambda_B$ < 803−804 nm in agreement with time-domain data.[36−38,60,70] $T_1$ values calculated from ZPHs are also in qualitative agreement with pump-probe[36,38,70] and 2DES data[37,60] (see green diamonds and asterisk) within the 812−818 nm region. For example, the average exciton lifetime calculated at 800 ± 0.5 nm (based on H **II**′) is ∼230 fs, but the maximum of the time distribution is near 80 fs (see Figure 9B). We assign the femtosecond components to a rapid loss of absorption, i.e., EET from excitonic states located near 12 420−12 500 $cm^{-1}$ to the lowest energy exciton state in agreement with pump-probe experiments[36,38,70] and 2DES data,[37,60] which revealed extremely short-lived ∼40−200 fs[37] *intramonomer* EET times of higher-energy (>12 460 $cm^{-1}$) excitons. In contrast, the $T_1$ values calculated with H **I**/H **II** were slower (see Figure S6 in the Supporting Information) and in poor agreement with frequency- (this work) and time-domain data, although, as shown in Figure 6A, the fits of the optical spectra for H **I** are very good. Calculated and experimentally observed sub-picosecond exciton lifetimes are also consistent with experimental $T_1$ values measured in *C. tepidum* FMO and its several mutants.[51] Thus, intramonomer energy transfer is found to proceed largely on sub-picosecond time scales with higher-exciton states extremely short lived, in qualitative agreement with 2DES experiments reported for *C. tepidum* FMO.[37,60] However, we cannot exclude that additional small changes in coupling constants could further improve agreement with experimental data. Thus, due to a large number of interdependent parameters, it is unworkable to pinpoint exact values of site energies (i.e., average values and distribution widths). This is not surprising since site-energy distributions, site-dependent spectral densities, and distributions in coupling matrix elements ($V_{n,m}$) cannot be exactly calculated, while all are very important in the optimization of EET.

In summary, we emphasize that very short exciton lifetimes are associated with very broad and shallow ZPHs,[24] as a result such holes cannot be easily observed by NPHB spectroscopy as HB quantum yield decreases for very short $T_1$ values. Thus, exciton lifetimes calculated from ZPHs likely represent an upper limit of $T_1$ values. Although resonant HB spectra cannot directly reveal a "multibranching", interconnected network of transfer into a number of other states, they reveal that the excited-state lifetimes are wavelength-dependent, with wavelength-dependent distributions, and cover broad fs to ps time scale. We believe that the calculated multimodal and asymmetric wavelength-dependent $T_1$ distributions may shed more light on the interpretation of time-domain data. However, research is still needed to show the wavelength-dependent distributions of exciton lifetimes within the 818−830 nm spectral range, work which is beyond the scope of this manuscript (research in progress).

**4.6. Comparison of BChl Site Energies.** Figure 12A compares simulation extracted site energies from ref 25 (blue squares) and ref 9 (red circles) with the recently calculated site energies by Saito et al.[17] (*P. aestuarii* FMO; blue triangles), using the MMSIC method, and Kim et al.[18] (black pentagons obtained for *C. tepidum* FMO). Kim et al. used classical MD simulations followed by partial correction of pigment structures by constrained QM/MM geometry optimization; electronic states were calculated with the TD-DFT PBE0/6−31G(d) approach.[18] Notably, the trend in calculated and simulation extracted site-dependent energies (this work; see frame B) is similar, except for BChls 2 and 8. Some of the observed differences might be attributed to variations between species. However, the calculated values are higher than those obtained from the simulations of optical spectra.[9,25] We hasten to add that site energies plotted in Figure 12A could not fit our data very well. Much better fits are obtained with site energies plotted in Figure 12B. Recall that both H **I**/H **II** and H **I**′/H **II**′ provided excellent fits of spectra shown in Figures 6A/B and 8A/B, respectively. For fits with H **III** and H **IV**, using a different set of optical spectra adopted from ref 12, see Figure S7 in the Supporting Information; site energies and inhomogeneities obtained for H **III** and H **IV** are plotted for comparison in Figures 12C and 13C, respectively (see also Tables S13/S15 in the Supporting Information). Our site-energy values are most similar to those calculated recently in refs 17 and 18. The calculated site energy for BChl 8 at 12 770 $cm^{-1}$ in ref 17 is similar to the previously calculated value for *P. aestuarii* FMO (i.e., 12 700 $cm^{-1}$, see Figure 12A).[9] These values, however, are significantly larger when compared with the results of oxidation experiments[7,8] and simultaneous fitting of multiple spectra shown in Figure S7. Interestingly, the recently[18] calculated site energy of BChl 8 near 12 475 $cm^{-1}$ (i.e., after its site energy using QM/effective fragment potential is shifted by −2430 $cm^{-1}$) is in very good agreement with our data (see Figure 12B) and oxidation experiments mentioned above. BChl 5 has a site energy much higher than that of the other chromophores in agreement with data reported in refs 9, 13, and 15. However, this is only the case for *P. aestuarii* as in *C. tepidum* FMO the highest energy was assigned to BChl 6.[8,13,20]

Note that the fitting of various optical spectra shown in Figures 6A/B, 8A/B, and S7 provided the same energetically ordered pigments (with similar site energies), which are moderately different from the data reported in refs 13, 15, 17, 25, and 71. Comparison of literature reported site energies for *P. aestuarii* is shown Table S14 in the Supporting Information.

**4.7. Comparison of Site-Dependent Inhomogeneities.** The local environment of the FMO protein surrounding a BChl produces disorder in site energies. At 5 K, slow thermal motion (compared to the BChl natural lifetime) of the protein is frozen, leading to inhomogeneous, or static, disorder. The top two sets of data in Figure 13A show the calculated $\Gamma_{inh}$ values obtained for *P. aestuarii* reported in refs 17 and 18, as blue triangles and yellow diamonds, respectively. The agreement is good, with the largest difference of about 50−80 $cm^{-1}$ calculated for BChls 1, 5, and 8. The black squares below correspond to $\Gamma_{inh}$ obtained from modeling studies discussed in ref 15. The blue asterisk indicates the fixed $\Gamma_{inh}$ value of 80 $cm^{-1}$ used for all BChls to fit


https://dx.doi.org/10.1021/acsomega.1c00286
ACS Omega 2021, 6, 5990−6008

spectra reported in ref 25. Figure 13B shows $\Gamma_{inh}$ values obtained from the modeling of spectra shown in Figures 6A (H **I**), 6B (H **II**), 8A (H **I′**), and 8B (H **II′**). Frame C in Figure 13 shows calculated $\Gamma_{inh}$ based on fits shown in Figures S7A (H **III**) and S7B (H **IV**). Interestingly, also in this case, the trend is similar to data plotted in frame B and data obtained by recent MD simulations (frame A) with the exception of $\Gamma_{inh}$ obtained for BChl 8 for which calculated $\Gamma_{inh}$ is significantly larger than that obtained to fit data shown in Figure S7. Although the $\Gamma_{inh}$ values revealed by all six Hamiltonians reported in this work are smaller in comparison with the values obtained via MD simulations, the trend is similar. It is likely that the calculated $\Gamma_{inh}$ values are larger since room-temperature MD simulations sample unique room-temperature conformations. This could be the reason why Saito et al.[17] could fit 300 K absorption but not the 77 K spectrum. We hasten to add that the authors of refs 17 and 18 used the calculated $\Gamma_{inh}$ values to fit both the 300 and 77 K spectra.

Since our site energies and $\Gamma_{inh}$ values fit well absorption spectra at both 5 and 77 K, we conclude that our Hamiltonians can be used to describe the electronic structure and dynamics of *P. aestuarii* FMO complexes at 5−77 K. That is, site energies and inhomogeneities (as calculated via MD simulations) should not be used to model low-temperature spectra, although it is very promising that the first principles-based calculations reproduce well the trend of both site-dependent energies and inhomogeneities.[17,18] In fact, disagreement between low- and high-temperature $\Gamma_{inh}$ values is expected since at low temperatures much protein motion is "frozen out" leading to smaller site inhomogeneities, in agreement with our modeling studies.

**4.8. Comparison of Exciton Energies.** Energy landscapes in *P. aestuarii* FMO based on H **I′** and H **II′** are illustrated graphically in Figure 14. (Nearly identical energy landscape was

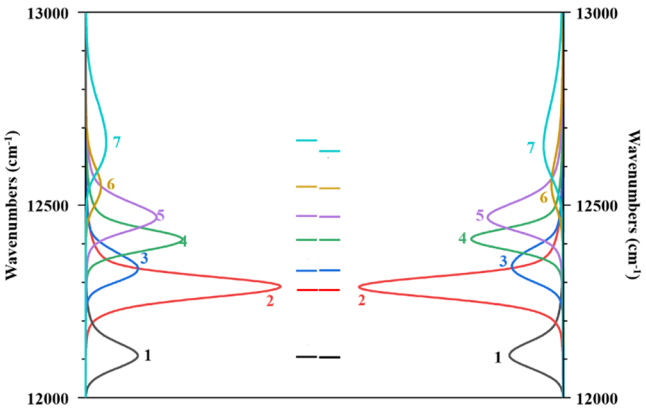


**Figure 14.** Seven exciton states were calculated for *P. aestuarii* monomer based on the optical spectra fitted using H **I′** (left; two SDs) and H **II′** (right; seven SDs) Hamiltonians, respectively. Short straight lines in the center show averaged energies of the corresponding excitonic states.

observed for H **I** and H **II**; data not shown.) That is, the disorder-averaged exciton states (obtained based on the fits of spectra shown in Figures 8A (two SDs) and 8B (seven SDs)) are plotted on the left and right side of Figure 14, respectively. Calculations are performed for monomers of the FMO trimer. All three monomer subunits within the trimer are assumed to be identical (with identical SDFs). In this case, the intermonomer coupling is neglected. Plotting exciton energy distributions (ranked from lowest to highest energy) for the 21 exciton states of the trimer would lead to a triple splitting of each excitonic state (data not shown for brevity). However, as an example, Figure S1 in the SI shows the abovementioned splitting for the 825 nm band calculated with H **I** and H **II**. Averaged exciton band energies (horizontal bars) are plotted in the center for an easy comparison.

Note that similar energies of exciton states are obtained, though the use of seven SD shifts averaged energy levels of excitons 5, 6, and 7 somewhat to lower energies. The largest difference is observed for exciton 7. For contribution numbers ($|c_{mM}|^2$) of pigments $m$ to monomeric excitonic states $M$, see Tables S3 and S4 in the SI. (Exciton states calculated using Hamiltonians H **III** and H **IV** (for fits shown in Figure S7) are given in Figure S8 for comparison.)

**4.9. Effect of Spectral Densities on Population Dynamics.** Very recently, by considering the fluctuations of the external electrostatic potential and BChl structure, it was shown that the spectral densities of individual BChls can be obtained theoretically.[17,72] As discussed above, the authors of refs 17 and 18 found site-dependent static disorder due to the local protein environment with a similar trend in relative values obtained in our modeling studies. As shown in Figure 10B, population dynamic calculations with seven (slightly modified) SDs from ref 17 provide faster dynamics, which is in better agreement with time-domain data.[37] In the non-Markovian density matrix theory, the EET rates between excitons depend on the amplitude of spectral densities at the exciton energy gap.[60] Thus, both higher average S-factors and shapes of the modified SDs facilitate faster population dynamics. Recall that both set of SDs discussed above provided good fits of low-T optical spectra (Figures 6A/B and 8A/B) with a small deviation in pigment site energies and $\Gamma_{inh}$ values as illustrated in Figures 12B and 13B (see Tables S13 and S15 for details). The latter is not surprising considering that the optical spectra of FMO are characterized by both relatively small electron−phonon coupling and large site-dependent inhomogeneous broadening. Thus, very good fits to various types of optical spectra are not enough to suggest that a corresponding Hamiltonian properly describes the system. It is necessary to provide a proper account of the experimentally observed exciton lifetimes. Based on the calculated population dynamics and averaged exciton lifetimes, we suggest that H **II′** is most consistent with HB (this work) and the time-domain data.[38,73,74] However, more experimental data and application of more advanced theories to simultaneously describe the dynamics in the entire $Q_y$-region could potentially provide a better Hamiltonian. Summarizing, Figure 15 shows the dominant channels of EET in a monomer of *P. aestuarii* complex calculated using the density matrix approach for H **II′**. We suggest that site-dependent spectral densities and coupling matrix elements are critical to describe simultaneously frequency- and time-domain data obtained for various light-harvesting photosynthetic antennas.

## 5. CONCLUDING REMARKS

Based on the modeling study of various low-temperature optical spectra reported above, we believe that all *P. aestuarii* FMO trimers studied in this work, as most FMO trimers whose data were reported in the literature,[21,22,25,75] contained 21 BChl per trimer. However, *P. aestuarii* complexes studied by Vulto et al.,[12,36] briefly discussed in the Supporting Information, could most likely contain a full occupation of BChl 8 (i.e., 24 BChls per trimer). Unfortunately, none of the samples studied in our laboratory showed similar absorption spectra revealing the


https://dx.doi.org/10.1021/acsomega.1c00286
ACS Omega 2021, 6, 5990−6008

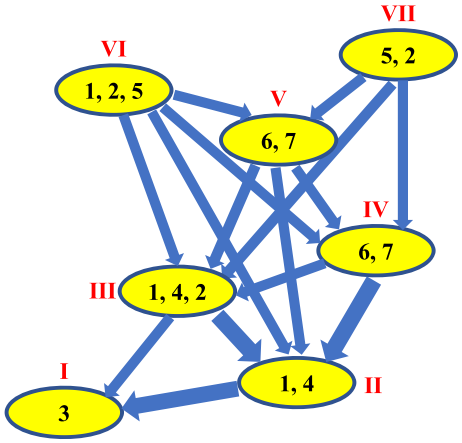


**Figure 15.** Schematic illustration of different (averaged) excitons and the dominant channels of EET in a monomer of *P. aestuarii* calculated using the density matrix approach and H **II**′. Thin and thick arrows show EET channels with rates contributing 15−50 and >50%, respectively. Roman numerals label excitonic states; Arabic numerals indicate ≥15% contribution of BChls to a particular exciton state in order of decreasing contribution (see Table S4).

presence of BChl 8. A comparison of data for complexes with 21 and 24 pigments per trimer allowed to elucidate the site energy of BChl 8 near ∼12 425 $cm^{-1}$ (∼805 nm). This energy is very similar to that observed for *C. tepidum* FMO with the main oxidative bleach observed near 12 407−12 422 $cm^{-1}$,[8] but very different from the theoretical values (12 750−13 900 $cm^{-1}$) reported recently in refs 17 and 18 Interestingly, the recently[18] calculated site energy of BChl 8 near 12 475 $cm^{-1}$ is in very good agreement with our modeling studies and oxidation experiments. As BChl *a* 8 is located at the interface between protein subunits and is very weakly coupled with the remaining pigments, it may be lost during FMO isolation/purification processes. It is not clear, however, to what extent the loss of BChl 8 destabilizes the FMO trimer. Besides, we cannot entirely exclude that naturally occurring trimers are very heterogeneous and contain variable number of BChls per complex. Therefore, optical spectra of both 21 and 24 BChls per trimer were analyzed theoretically; both trimers have similar BChl site energies and pigment-dependent inhomogeneities.

Two sets of different spectral densities revealed how their shapes affect the population dynamics and exciton lifetime distributions. As a result, four Hamiltonians are discussed. The latter allowed the calculation of average exciton lifetimes that are compared with relaxation times obtained in this work, via resonant HB, and with the literature data obtained by femtosecond one- and two-color pump-probe measurements[36,38] and 2DES experiments.[37,60,76] We emphasize that exciton lifetimes obtained from the resonant HB spectra may not be directly comparable with the calculated averaged $T_1$ values, since low-fluence, resonant holes do not probe the entire exciton lifetime distribution. Nevertheless, the HB data are in good agreement with pump-probe measurements.[36,38] The experimental values constrain which combination of spectral densities (i.e., which Hamiltonian) provides most reliable site energies of individual BChls and their standard deviations at low temperature (i.e., the inhomogeneous broadening). While all four Hamiltonians tested in this work provided similar site energies and inhomogeneous broadenings as illustrated in Figures 12 and 13 (see also Tables S1, S2, S7, and S8), only H **II**′ (with slightly modified coupling constants) provides a reasonable agreement between frequency- and time-domain data, at least within the 802−816 nm region. Thus, we suggest that H **II**′ with seven modified spectral densities provides a better description of exciton structure and relaxation dynamics for *P. aestuarii* with 21 BChls per trimer. In turn, Hamiltonian **IV** (discussed briefly in the Supporting Information) seems to be most consistent with data describing FMO complexes with 24 BChls per trimer. Finally, in agreement with theoretical calculations,[18] BChls 2 and 5 in all our Hamiltonians have highest site energies; however, we do not find any evidence that the site energy of BChl 8 has very high energy as suggested by theoretical calculations reported in refs 9 and 17. Most importantly, however, our algorithm simultaneously fitting multiple spectra revealed a similar trend of the distribution of site energies (and inhomogeneities) of the individual sites in good agreement with calculations reported recently in refs 17 and 18. That is, narrowest distributions are obtained for BChls 1, 3, 4, 6, and 7 and broadest distributions for BChls 2 and 5, although calculated distributions (via MD simulations) are larger than those obtained from our modeling studies.[17,18] However, we suggest that site-energy fluctuations revealed via MD simulations are more appropriate to model room-temperature spectra. In fact, disagreement between low- and high-temperature $\Gamma_{inh}$ values was expected since at low temperatures much protein motion is "frozen out" leading to smaller site inhomogeneities. The fact that better agreement between frequency- and time-domain data (within the 800−818 nm spectral range) is provided using H **II**′ (which slightly modifies coupling constants) suggests that TrEsp calculated $V_{n,m}$ parameters are not perfect and future modeling should include their distributions.

In summary, we conclude that although simultaneously fitted multiple spectra provide more constraints on the resulting excitonic structure, very good fits of multiple optical spectra may not be sufficient to determine optimal Hamiltonians. Additional frequency- and time-domain data are needed to provide more consistent description of excitonic structure and exciton lifetimes. In addition, more advanced theories should be used to describe the experimental data shown in Figure 7. Although the resonant HB spectra cannot reveal a multibranching, interconnected network of transfer into a number of other states, resonant HB spectra provide average excited-state lifetimes $T_1$, which are strongly wavelength dependent. These averages, however, do not have to be identical to the calculated averaged $T_1$ values since the latter values calculated using the non-Markovian density matrix approach do not take into account differences in HB quantum yield ($\phi$), which not only depend on excitons and fluorescence lifetimes but also on the tunneling parameter ($\lambda$). Unfortunately, the tunneling parameter rate, which depends on $\lambda$ as $\exp(-2\lambda)$,[77] and distribution of $\lambda$ are unknown. That is, tunneling in the excited state that is the dominant process responsible for NPHB processes may also change across the absorption bands due to the very complex energy landscape in the protein configurational space. Nevertheless, calculations revealed multimodal, wavelength-dependent distributions in the fs to ps time frame in reasonable agreement with experimental data. We suggest that the multimodal and asymmetric, wavelength-dependent $T_1$ distributions could be compared with the future two-dimensional matrix of kinetic traces in 2DES experiments for *P. aestuarii*, possibly offering more insight on the interpretation of $T_1$ values obtained from the resonant holes burned across the absorption spectrum.


https://dx.doi.org/10.1021/acsomega.1c00286
*ACS Omega* 2021, 6, 5990−6008

## ■ ASSOCIATED CONTENT

### Supporting Information

The Supporting Information is available free of charge at https://pubs.acs.org/doi/10.1021/acsomega.1c00286.

Redfield and Förster theories; lowest-energy exciton states of a trimer of the FMO complex; intermonomer energy transfer times in the FMO complex calculated using generalized Förster theory for Hamiltonians **I** and **II**; modified Drude−Lorentz SDs; contributions from trimer and monomers; BChl contributions to the calculated optical spectra; fits of multiple optical spectra from Vulto et al., 1998; and tables comparing site energies and inhomogeneities from present work and literature data (PDF)

## ■ AUTHOR INFORMATION


### Corresponding Author

**Ryszard Jankowiak** − *Department of Chemistry and Department of Physics, Kansas State University, Manhattan, Kansas 66506, United States;* orcid.org/0000-0003-3302-9232; Phone: 785-532-6785; Email: ryszard@ksu.edu

### Authors

**Tonu Reinot** − *Department of Chemistry, Kansas State University, Manhattan, Kansas 66506, United States*

**Anton Khmelnitskiy** − *Department of Chemistry, Kansas State University, Manhattan, Kansas 66506, United States*

**Adam Kell** − *Department of Chemistry, Kansas State University, Manhattan, Kansas 66506, United States*

**Mahboobe Jassas** − *Department of Chemistry, Kansas State University, Manhattan, Kansas 66506, United States*

Complete contact information is available at: https://pubs.acs.org/10.1021/acsomega.1c00286


### Notes

The authors declare no competing financial interest.

## ■ ACKNOWLEDGMENTS

U.S. Department of Energy, Office of Science, Office of Basic Energy Sciences, supported this work under Award Number DE-SC-0006678 (to R.J.). We acknowledge Dr. R. E. Blankenship and his students/postdoctoral fellows from Departments of Chemistry and Biology, Washington University in St. Louis, St. Louis, MO 63130 (United States) who kindly provided the FMO samples for our research during the last decade. We also acknowledge Dr. Khem Acharya who was involved in our experimental efforts at the very early stage of this work.

## ■ REFERENCES


(1) Li, Y.-F.; Zhou, W.; Blankenship, R. E.; Allen, J. P. Crystal Structure of the Bacteriochlorophyll a Protein from *Chlorobium tepidum*. *J. Mol. Biol.* **1997**, *271*, 456−471.

(2) Tronrud, D. E.; Wen, J.; Gay, L.; Blankenship, R. E. The Structural Basis for the Difference in Absorbance Spectra for the FMO Antenna Protein from Various Green Sulfur Bacteria. *Photosynth. Res.* **2009**, *100*, 79−87.

(3) Lu, X.; Selvaraj, B.; Ghimire-Rijal, S.; Orf, G. S.; Meilleur, F.; Blankenship, R. E.; Cuneo, M. J.; Myles, D. A. A. Neutron and X-Ray Analysis of the Fenna−Matthews−Olson Photosynthetic Antenna Complex from *Prosthecochloris aestuarii*. *Acta Crystallogr., Sect. F: Struct. Biol. Cryst. Commun.* **2019**, *75*, 171−175.

(4) Tronrud, D. E.; Schmid, M. F.; Matthews, B. W. Structure and X-Ray Amino Acid Sequence of a Bacteriochlorophyll a Protein from *Prosthecochloris aestuarii* Refined at 1.9 Å Resolution. *J. Mol. Biol.* **1986**, *188*, 443−454.

(5) Fenna, R. E.; Matthews, B. W. Chlorophyll Arrangement in a Bacteriochlorophyll Protein from *Chlorobium limicola*. *Nature* **1975**, *258*, 573−577.

(6) Tronrud, D. E.; Allen, J. P. Reinterpretation of the Electron Density at the Site of the Eighth Bacteriochlorophyll in the FMO Protein from *Pelodictyon phaeum*. *Photosynth. Res.* **2012**, *112*, 71−74.

(7) Niedzwiedzki, D. M.; Bina, D.; Picken, N.; Honkanen, S.; Blankenship, R. E.; Holten, D.; Cogdell, R. J. Spectroscopic Studies of Two Spectral Variants of Light-Harvesting Complex 2 (LH2) from the Photosynthetic Purple Sulfur Bacterium *Allochromatium vinosum*. *Biochim. Biophys. Acta, Bioenerg.* **2012**, *1817*, 1576−1587.

(8) Kell, A.; Blankenship, R. E.; Jankowiak, R. Effect of Spectral Density Shapes on the Excitonic Structure and Dynamics of the Fenna−Matthews−Olson Trimer from *Chlorobaculum tepidum*. *J. Phys. Chem. A* **2016**, *120*, 6146−6154.

(9) Schmidt am Busch, M.; Müh, F.; El-Amine Madjet, M.; Renger, T. The Eighth Bacteriochlorophyll Completes the Excitation Energy Funnel in the FMO Protein. *J. Phys. Chem. Lett.* **2011**, *2*, 93−98.

(10) Olbrich, C.; Strümpfer, J.; Schulten, K.; Kleinekathöfer, U. Quest for Spatially Correlated Fluctuations in the FMO Light-Harvesting Complex. *J. Phys. Chem. B* **2011**, *115*, 758−764.

(11) Olbrich, C.; Strümpfer, J.; Schulten, K.; Kleinekathöfer, U. Theory and Simulation of the Environmental Effects on FMO Electronic Transitions. *J. Phys. Chem. Lett.* **2011**, *2*, 1771−1776.

(12) Vulto, S. I. E.; de Baat, M. A.; Louwe, R. J. W.; Permentier, H. P.; Neef, T.; Miller, M.; van Amerongen, H.; Aartsma, T. J. Exciton Simulations of Optical Spectra of the FMO Complex from the Green Sulfur Bacterium *Chlorobium tepidum* at 6 K. *J. Phys. Chem. B* **1998**, *102*, 9577−9582.

(13) Adolphs, J.; Renger, T. How Proteins Trigger Excitation Energy Transfer in the FMO Complex of Green Sulfur Bacteria. *Biophys. J.* **2006**, *91*, 2778−2797.

(14) Gülen, D. Interpretation of the Excited-State Structure of the Fenna−Matthews−Olson Pigment Protein Complex of *Prosthecochloris aestuarii* Based on the Simultaneous Simulation of the 4 K Absorption, Linear Dichroism, and Singlet−Triplet Absorption Difference Spectra. *J. Phys. Chem. A.* **1996**, *100*, 17683−17689.

(15) Müh, F.; Madjet, M. E.-A.; Adolphs, J.; Abdurahman, A.; Rabenstein, B.; Ishikita, H.; Knapp, E.-W.; Renger, T. Alpha-Helices Direct Excitation Energy Flow in the Fenna Matthews Olson Protein. *Proc. Natl. Acad. Sci. U.S.A.* **2007**, *104*, 16862−16867.

(16) Adolphs, J.; Müh, F.; Madjet, M. E. A.; Renger, T. Calculation of Pigment Transition Energies in the FMO Protein: From Simplicity to Complexity and Back. *Photosynth. Res.* **2008**, *95*, 197−209.

(17) Saito, S.; Higashi, M.; Fleming, G. R. Site-Dependent Fluctuations Optimize Electronic Energy Transfer in the Fenna−Matthews−Olson Protein. *J. Phys. Chem. B* **2019**, *123*, 9762−9772.

(18) Kim, Y.; Morozov, D.; Stadnytskyi, V.; Savikhin, S.; Slipchenko, L. V. Predictive First-Principles Modeling of a Photosynthetic Antenna Protein: The Fenna-Matthews-Olson Complex. *J. Phys. Chem. Lett.* **2020**, *11*, 1636−1643.

(19) Milder, M. T. W.; Brüggemann, B.; van Grondelle, R.; Herek, J. L. Revisiting the Optical Properties of the FMO Protein. *Photosynth. Res.* **2010**, *104*, 257−274.

(20) Khmelnitskiy, A.; Kell, A.; Reinot, T.; Saer, R. G.; Blafnkenship, R. E.; Jankowiak, R. Energy Landscape of the Intact and Destabilized FMO Antennas from *C. tepidum* and the L122Q Mutant: Low Temperature Spectroscopy and Modeling Study. *Biochim. Biophys. Acta, Bioenerg.* **2018**, *1859*, 165−173.

(21) Franken, E. M.; Neerken, S.; Louwe, R. J. W.; Amesz, J.; Aartsma, T. J. A Permanent Hole Burning Study of the FMO Antenna Complex of the Green Sulfur Bacterium *Prosthecochloris aestuarii*. *Biochemistry* **1998**, *37*, 5046−5051.

(22) Matsuzaki, S.; Zazubovich, V.; Rätsep, M.; Hayes, J. M.; Small, G. J. Energy Transfer Kinetics and Low Energy Vibrational Structure of the Three Lowest Energy Qy -States of the Fenna−Matthews−Olson Antenna Complex. *J. Phys. Chem. B* **2000**, *104*, 9564−9572.

(23) Johnson, S.; Small, G. Excited-State Structure and Energy-Transfer Dynamics of the Bacteriochlorophyll a Antenna Complex from *Prosthecochloris aestuarii*. *J. Phys. Chem. B.* **1991**, *95*, 471−479.
(24) Jankowiak, R.; Reppert, M.; Zazubovich, V.; Pieper, J.; Reinot, T. Site Selective and Single Complex Laser-Based Spectroscopies: A Window on Excited State Electronic Structure, Excitation Energy Transfer, and Electron-Phonon Coupling of Selected Photosynthetic Complexes. *Chem. Rev.* **2011**, *111*, 4546−4598.
(25) Wendling, M.; Przyjalgowski, M. A.; Gülen, D.; Vulto, S. I. E.; Aartsma, T. J.; van Grondelle, R.; van Amerongen, H. The Quantitative Relationship between Structure and Polarized Spectroscopy in the FMO Complex of *Prosthecochloris aestuarii*: Refining Experiments and Simulations. *Photosynth. Res.* **2002**, *71*, 99−123.
(26) Duan, H.-G.; Prokhorenko, V. I.; Cogdell, R. J.; Ashraf, K.; Stevens, A. L.; Wientjes, E.; Croce, R.; Thorwart, M.; Miller, R. J. D. Lack of Long-Lived Quantum Coherence in the Photosynthetic Energy Transfer. *EPJ Web Conf.* **2019**, *205*, 09035.
(27) Savikhin, S.; Zhou, W.; Blankenship, R. E.; Struve, W. S. Femtosecond Energy Transfer and Spectral Equilibration in Bacteriochlorophyll A–Protein Antenna Trimers from the Green Bacterium *Chlorobium tepidum*. *Biophys. J.* **1994**, *66*, 110−113.
(28) Engel, G. S.; Calhoun, T. R.; Read, E. L.; Ahn, T.-K.; Mancal, T.; Cheng, Y.-C.; Blankenship, R. E.; Fleming, G. R. Evidence for Wavelike Energy Transfer through Quantum Coherence in Photosynthetic Systems. *Nature* **2007**, *446*, 782−786.
(29) Mohseni, M.; Rebentrost, P.; Lloyd, S.; Aspuru-Guzik, A. Environment-Assisted Quantum Walks in Photosynthetic Energy Transfer. *J. Chem. Phys.* **2008**, *129*, No. 174106.
(30) Ritschel, G.; Roden, J.; Strunz, W. T.; Aspuru-Guzik, A.; Eisfeld, A. Absence of Quantum Oscillations and Dependence on Site Energies in Electronic Excitation Transfer in the Fenna-Matthews-Olson Trimer. *J. Phys. Chem. Lett.* **2011**, *2*, 2912−2917.
(31) Christensson, N.; Kauffmann, H. F.; Pullerits, T.; Mančal, T. Origin of Long-Lived Coherences in Light-Harvesting Complexes. *J. Phys. Chem. B* **2012**, *116*, 7449−7454.
(32) Rätsep, M.; Blankenship, R. E.; Small, G. J. Energy Transfer and Spectral Dynamics of the Three Lowest Energy Q(y)-States of the Fenna-Matthews-Olson Antenna Complex. *J. Phys. Chem. B* **1999**, *103*, 5736−5741.
(33) Khmelnitskiy, A.; Jankowiak, R. Impact of Single Point Mutations on the Excitonic Structure and Dynamics in FMO Complex. *EPJ Web Conf.* **2018**, *190*, 02005.
(34) Kell, A.; Acharya, K.; Blankenship, R. E.; Jankowiak, R. On Destabilization of the Fenna-Matthews-Olson Complex of *Chlorobaculum tepidum*. *Photosynth. Res.* **2014**, *120*, 323−329.
(35) Bina, D.; Blankenship, R. E. Chemical Oxidation of the FMO Antenna Protein from *Chlorobaculum tepidum*. *Photosynth. Res.* **2013**, *116*, 11−19.
(36) Vulto, S. I. E.; Streltsov, A. M.; Aartsma, T. J. Excited State Energy Relaxation in the FMO Complexes of the Green Bacterium *Prosthecochloris aestuarii* at Low Temperatures. *J. Phys. Chem. B* **1997**, *101*, 4845−4850.
(37) Thyrhaug, E.; Žídek, K.; Dostál, J.; Bína, D.; Zigmantas, D. Exciton Structure and Energy Transfer in the Fenna−Matthews−Olson Complex. *J. Phys. Chem. Lett.* **2016**, *7*, 1653−1660.
(38) Savikhin, S.; Struve, W. S. Ultrafast Energy Transfer in FMO Trimers from the Green Bacterium *Chlorobium tepidum*. *Biochemistry* **1994**, *33*, 11200−11208.
(39) Wen, J.; Zhang, H.; Gross, M. L.; Blankenship, R. E. Membrane Orientation of the FMO Antenna Protein from *Chlorobaculum tepidum* as Determined by Mass Spectrometry-Based Footprinting. *Proc. Natl. Acad. Sci. U.S.A.* **2009**, *106*, 6134−6139.
(40) Wen, J.; Harada, J.; Buyle, K.; Yuan, K.; Tamiaki, H.; Oh-Oka, H.; Loomis, R. A.; Blankenship, R. E. Characterization of an FMO Variant of *Chlorobaculum tepidum* Carrying Bacteriochlorophyll a Esterified by Geranylgeraniol. *Biochemistry* **2010**, *49*, 5455−5463.
(41) Kell, A.; Feng, X.; Reppert, M.; Jankowiak, R. On the Shape of the Phonon Spectral Density in Photosynthetic Complexes. *J. Phys. Chem. B* **2013**, *117*, 7317−7323.
(42) Rätsep, M.; Freiberg, A. Electron-Phonon and Vibronic Couplings in the FMO Bacteriochlorophyll a Antenna Complex Studied by Difference Fluorescence Line Narrowing. *J. Lumin.* **2007**, *127*, 251−259.
(43) Renger, T.; Madjet, M. E.; Knorr, A.; Müh, F. How the Molecular Structure Determines the Flow of Excitation Energy in Plant Light-Harvesting Complex II. *J. Plant Physiol.* **2011**, *168*, 1497−1509.
(44) Renger, T.; Marcus, R. A. On the Relation of Protein Dynamics and Exciton Relaxation in Pigment−Protein Complexes: An Estimation of the Spectral Density and a Theory for the Calculation of Optical Spectra. *J. Chem. Phys.* **2002**, *116*, 9997−10019.
(45) Nelder, J. A.; Mead, R. A Simplex Method for Function Minimization. *Comput. J.* **1965**, *7*, 308−313.
(46) Redfield, A. G. On the Theory of Relaxation Processes. *IBM J. Res. Dev.* **1957**, *1*, 19−31.
(47) Wendling, M.; Pullerits, T.; Przyjalgowski, M. A.; Vulto, S. I. E.; Aartsma, T. J.; van Grondelle, R.; van Amerongen, H. Electron Vibrational Coupling in the Fenna Matthews Olson Complex of *Prosthecochloris aestuarii* Determined by Temperature Dependent Absorption and Fluorescence Line-Narrowing Measurements. *J. Phys. Chem. B* **2000**, *104*, 5825−5831.
(48) Kell, A.; Acharya, K.; Zazubovich, V.; Jankowiak, R. On the Controversial Nature of the 825 Nm Exciton Band in the FMO Protein Complex. *J. Phys. Chem. Lett.* **2014**, *5*, 1450−1456.
(49) Kell, A.; Khmelnitskiy, A. Y.; Reinot, T.; Jankowiak, R. On Uncorrelated Inter-Monomer Förster Energy Transfer in Fenna−Matthews−Olson Complexes. *J. R. Soc., Interface* **2019**, *16*, No. 20180882.
(50) Jankowiak, R.; Hayes, J. M.; Small, G. J. Spectral Hole-Burning Spectroscopy in Amorphous Molecular Solids and Proteins. *Chem. Rev.* **1993**, *93*, 1471−1502.
(51) Khmelnitskiy, A.; Reinot, T.; Jankowiak, R. Impact of Single-Point Mutations on the Excitonic Structure and Dynamics in a Fenna−Matthews−Olson Complex. *J. Phys. Chem. Lett.* **2018**, *9*, 3378−3386.
(52) Madjet, M. E.; Abdurahman, A.; Renger, T. Intermolecular Coulomb Couplings from Ab Initio Electrostatic Potentials: Application to Optical Transitions of Strongly Coupled Pigments in Photosynthetic Antennae and Reaction Centers. *J. Phys. Chem. B* **2006**, *110*, 17268−17281.
(53) Thyrhaug, E.; Tempelaar, R.; Alcocer, M. J. P.; Žídek, K.; Bína, D.; Knoester, J.; Jansen, T. L. C.; Zigmantas, D. Identification and characterization of diverse coherences in the Fenna−Matthews−Olson complex. *Nat. Chem.* **2018**, *10*, 780−786.
(54) Vulto, S. I. E.; de Baat, M. A.; Neerken, S.; Nowak, F. R.; van Amerongen, H.; Amesz, J.; Aartsma, T. J. Excited State Dynamics in FMO Antenna Complexes from Photosynthetic Green Sulfur Bacteria: A Kinetic Model. *J. Phys. Chem. B* **1999**, *103*, 8153−8161.
(55) Jassas, M.; Chen, J.; Khmelnitskiy, A.; Casazza, A. P.; Santabarbara, S.; Jankowiak, R. Structure-Based Exciton Hamiltonian and Dynamics for the Reconstituted Wild-Type CP29 Protein Antenna Complex of the Photosystem II. *J. Phys. Chem. B* **2018**, *122*, 4611−4624.
(56) Reinot, T.; Chen, J.; Kell, A.; Jassas, M.; Robben, K. C.; Zazubovich, V.; Jankowiak, R. On the Conflicting Estimations of Pigment Site Energies in Photosynthetic Complexes: A Case Study of the CP47 Complex. *Anal. Chem. Insights* **2016**, *11*, No. ACI.S32151.
(57) Kell, A.; Bednarczyk, D.; Acharya, K.; Chen, J.; Noy, D.; Jankowiak, R. New Insight into the Water-Soluble Chlorophyll-Binding Protein from *Lepidium virginicum*. *Photochem. Photobiol.* **2016**, *92*, 428−435.
(58) Mančal, T. Excitation Energy Transfer in a Classical Analogue of Photosynthetic Antennae. *J. Phys. Chem. B* **2013**, *117*, 11282−11291.
(59) Reppert, M.; Brumer, P. Quantumness in Light Harvesting Is Determined by Vibrational Dynamics. *J. Chem. Phys.* **2018**, *149*, No. 234102.
(60) Cho, M.; Vaswani, H. M.; Brixner, T.; Stenger, J.; Fleming, G. R. Exciton Analysis in 2D Electronic Spectroscopy. *J. Phys. Chem. B* **2005**, *109*, 10542−10556.


https://dx.doi.org/10.1021/acsomega.1c00286
*ACS Omega* 2021, 6, 5990−6008

(61) Toutounji, M. M.; Small, G. J. The Underdamped Brownian Oscillator Model with Ohmic Dissipation: Applicability to Low-Temperature Optical Spectra. *J. Chem. Phys.* **2002**, *117*, 3848−3855.
(62) Khmelnitskiy, A.; Saer, R. G.; Blankenship, R. E.; Jankowiak, R. Excitonic Energy Landscape of the Y16F Mutant of the *Chlorobium tepidum* Fenna−Matthews−Olson (FMO) Complex: High Resolution Spectroscopic and Modeling Studies. *J. Phys. Chem. B* **2018**, *122*, 3734−3743.
(63) Creemers, T. M.; Caro, C.; Visschers, R. W.; van Grondelle, R.; Völker, S. Spectral Hole Burning and Fluorescence Line Narrowing in Subunits of the Light Harvesting Complex LH1 of Purple Bacteria. *J. Phys. Chem. B* **1999**, *103*, 9770−9776.
(64) Louwe, R. J. W.; Aastsma, T. J. Optical Dephasing and Excited State Dynamics in Photosynthetic Pigment-Protein Complexes. *J. Lumin.* **1994**, *58*, 154−157.
(65) Raszewski, G.; Renger, T. Light Harvesting in Photosystem II Core Complexes Is Limited by the Transfer to the Trap: Can the Core Complex Turn into a Photoprotective Mode? *J. Am. Chem. Soc.* **2008**, *130*, 4431−4446.
(66) Renger, T.; Müh, F. Understanding Photosynthetic Light-Harvesting: A Bottom up Theoretical Approach. *Phys. Chem. Chem. Phys.* **2013**, *15*, 3348−3371.
(67) Duan, H.-G.; Prokhorenko, V. I.; Cogdell, R. J.; Ashraf, K.; Stevens, A. L.; Thorwart, M.; Miller, R. J. D. Nature Does Not Rely on Long-Lived Electronic Quantum Coherence for Photosynthetic Energy Transfer. *Proc. Natl. Acad. Sci. U.S.A.* **2017**, *114*, 8493−8498.
(68) Higashi, M.; Saito, S. Quantitative Evaluation of Site Energies and Their Fluctuations of Pigments in the Fenna-Matthews-Olson Complex with an Efficient Method for Generating a Potential Energy Surface. *J. Chem. Theory Comput.* **2016**, *12*, 4128−4137.
(69) Reppert, M.; Acharya, K.; Neupane, B.; Jankowiak, R. Lowest Electronic States of the CP47 Antenna Protein Complex of Photosystem II: Simulation of Optical Spectra and Revised Structural Assignments. *J. Phys. Chem. B* **2010**, *114*, 11884−11898.
(70) Magdaong, N. C. M.; Saer, R. G.; Niedzwiedzki, D. M.; Blankenship, R. E. Ultrafast Spectroscopic Investigation of Energy Transfer in Site-Directed Mutants of the Fenna−Matthews−Olson (FMO) Antenna Complex from *Chlorobaculum tepidum*. *J. Phys. Chem. B* **2017**, *121*, 4700−4712.
(71) Iseri, E. I.; Gülen, D. Electronic Excited States and Excitation Transfer Kinetics in the Fenna- Matthews-Olson Protein of the Photosynthetic Bacterium *Prosthecochloris aestuarii* at Low Temperatures. *Eur. Biophys. J.* **1999**, *28*, 243−253.
(72) Higashi, M.; Saito, S. Quantitative Evaluation of Site Energies and Their Fluctuations of Pigments in the Fenna − Matthews − Olson Complex with an Efficient Method for Generating a Potential Energy Surface. *J. Chem. Theory Comput.* **2016**, *12*, 4128−4237.
(73) Thyrhaug, E.; Tempelaar, R.; Alcocer, M.; Žídek, K.; Bína, D.; Knoester, J.; Jansen, T. L. C.; Zigmantas, D. Unravelling Coherences in the FMO Complex. arXiv preprint arXiv:1709.00318. 2017, No. September.
(74) Vulto, S. I. E.; Neerken, S.; Louwe, R. J. W.; De Baat, M. A.; Amesz, J.; Aartsma, T. J. Excited-State Structure and Dynamics in FMO Antenna Complexes from Photosynthetic Green Sulfur Bacteria. *J. Phys. Chem. B* **1998**, *102*, 10630−10635.
(75) Beekman, L. M. P.; van Mourik, F.; Jones, M. R.; Visser, H. M.; Hunter, C. N.; van Grondelle, R. Trapping Kinetics in Mutants of the Photosynthetic Purple Bacterium Rhodobacter Sphaeroides: Influence of the Charge Separation Rate and Consequences for the Rate-Limiting Step in the Light-Harvesting Process. *Biochemistry* **1994**, *33*, 3143−3147.
(76) Brixner, T.; Stenger, J.; Vaswani, H. M.; Cho, M.; Blankenship, R. E.; Fleming, G. R. Two-Dimensional Spectroscopy of Electronic Couplings in Photosynthesis. *Nature* **2005**, *434*, 625−628.
(77) Najafi, M.; Herascu, N.; Seibert, M.; Picorel, R.; Jankowiak, R.; Zazubovich, V. Spectral Hole Burning, Recovery, and Thermocycling in Chlorophyll−Protein Complexes: Distributions of Barriers on the Protein Energy Landscape. *J. Phys. Chem. B* **2012**, *116*, 11780−11790.


https://dx.doi.org/10.1021/acsomega.1c00286
*ACS Omega* 2021, 6, 5990−6008